Table of Contents

List of Figures

Chapter 1: Introduction

1.1 Dark Matter

WIMPs ... ...

1.2 Dark Matter Detectors

Overview of field

1.3 Outline of Thesis

In Chap. 2, we present the results of a computational study of the influence of stochasticity on the dynamical evolution of multiple four-wave-mixing processes in a single mode optical fiber with spatially and temporally δ-correlated phase noise. A generalized nonlinear Schrödinger equation (NLSE) with stochastic phase fluctuations along the length of the fiber is solved using the Split-step Fourier method (SSFM). Good agreement is obtained with previous experimental and computational results based on a truncated-ODE (Ordinary Differential Equation) model in which stochasticity was seen to play a key role in determining the nature of the dynamics. The full NLSE allows for simulations with high frequency resolution (60 MHz) and frequency span (16 THz) compared to the truncated ODE model (300 GHz and 2.8 THz, respectively), thus enabling a more detailed comparison with observations. A physical basis for this hitherto phenomenological phase noise is discussed and quantified.

In Chap. 3, we discuss the implications of spontaneous and stimulated Raman scattering on the project discussed in Chap. 2, namely, the dynamical evolution of stochastic four-wave-mixing processes in an optical fiber. The following question is asked - can stimulated Raman scattering be a mechanism by which adequate multiplicative stochastic phase fluctuations are introduced in the electric field of light undergoing four-wave-mixing as? Adequately checked numerical algorithms of stimulated Raman scattering (SRS), spontaneous Raman generation and intrapulse Raman scattering (IRS) are used while exploring this issue. The algorithms are described in detail, as also are the results of the simulations. It is found that a 50-meter length of fiber (as used in the experiments), is too short to see the influence of Raman scattering, which is found to eventually dominate for longer fiber lengths.

In Chap. 4, self- and cross-phase modulation (XPM) of femtosecond pulses ($\sim$ 810 nm) propagating through a birefringent single-mode optical fiber ($\sim$ 6.9 cm) is studied both experimentally (using GRENOUILLE - Grating Eliminated No Nonsense Observation of Ultrafast Laser Light Electric Fields) and numerically (by solving a set of coupled nonlinear Schrödinger equations or CNLSEs). An optical spectrogram representation is derived from the electric field of the pulses and is linearly juxtaposed with the corresponding optical spectrum and optical time-trace. The effects of intrapulse Raman scattering (IRS) are discussed and the question whether it can be a cause of asymmetric tranfer of pulse energies towards longer wavelengths is explored. The simulations are shown to be in good qualitative agreement with the experiments. Measured input pulse asymmetry, when incorporated into the simulations, is found to be the dominant cause of output spectral asymmetry. [1] The results indicate that it is possible to modulate short pulses both temporally and spectrally by passage through polarization maintaining optical fibers with specified orientation and length. The modulation technique is very direct and straightforward. No frequency components of the broadband pulse have to be rejected as the entire spectrum is uniformly modulated. The technique is flexible as the modulation spacing can be varied by varying the fiber length.

Chapter 5 provides the conclusion to the thesis.

‘

[1] These averages are reported for 45 ‘detailed occupational codes’, which is an intermediate occupational classification (between two and three-digit codes) given by the Current Population Survey (CPS).

Chapter 2: The LUX Detector

2.1 Introduction

The LUX experiment is located 4850 ft underground at the Sanford Underground Research Facility. After running for 87 live days in 2013 LUX has recently set the most sensitive limit for a spin independent WIMP scattering cross section [ref] and is expected to achieve five times the sensitivity after a 300 day run in 2015. Nobel elements are ideal candidates for WIMP detection, they are easy to purify and are transparent to their own scintillation light. Xenon is especially favorable do to it's large atomic mass (131.3 amu) and high liquid phase density (sim2.9 kg/l) which provides both an excellent target for coherent WIMP scattering while simultaneously providing excellent shielding from external radioactivity. Xenon also has good radio purity with established techniques to remove and monitor troublesome radio isotopes of argon and krypton found in the atmosphere from which the xenon is distilled [refs]. WIMPs being electrically neutral would primarily interact with the xenon target nuclei producing nuclear recoils (NR) whereas typical backgrounds in the detector, gammas and betas, interact with the electrons producing electronic recoils (ER). In liquid xenon ER events can be further discriminated from NR events by about a factor of 1000 by taking the charge to light ratio of the interaction.

2.2 The LUX TPC

The LUX detector is a two phase xenon time projection chamber TPC, [ref LUX inst]. . The detector contains two PMT arrays on the top and bottom with 61 PMTs each for a total of 122 PMTs, with quantum efficiencies ranging from 30-40%. The active region consists of a 49 cm length between the cathode and gate with a 47 cm diameter of the dodecagonal geometry. The drift field between the cathode and gate is 180 V/cm resulting in an electron drift velocity of 1.51 mm/μs. The liquid level terminates 5-6mm above the gate grid as the liquid xenon spills over into a weir reservoir. The anode grid is placed 1.0 cm above the gate grid and used to setup the electron extraction field of 6 kV/cm where electrons are removed from the liquid and accelerated causing electroluminescence in the gas phase. LUX contains a gross 350 kg of xenon of which 250 kg are in the active region and 118 kg fiducial. A schematic of the detector in shown in ...

2.3 The Light and Charge Signals

When energy is deposited in the active region of the xenon TPC it is converted to excitation, ionization and heat, equation 2.1. For a given energy deposit, NR events lose a significant portion of energy to heat leaving less energy available for excitation and ionization than an ER event. Xenon excitons de-excite on the order of nano seconds producing 175nm VUV scintillation light, recombining ion electron pairs also emit scintillation light. The two channels for photon production overlap and

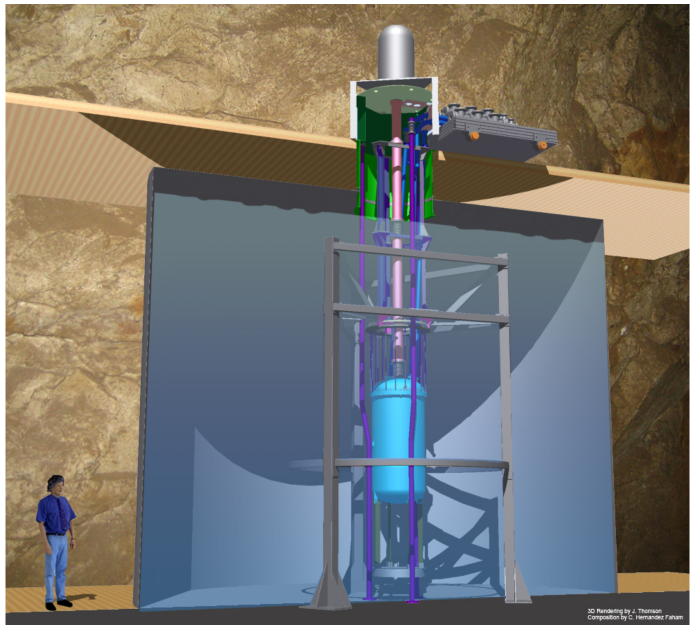

Figure 2.1: Schematic of the LUX detector and the surrounding water tank.

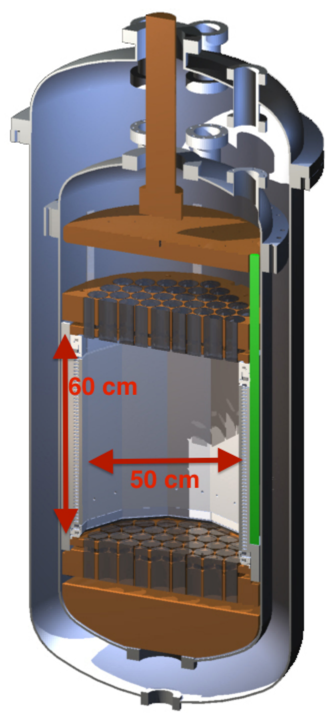

Figure 2.2: LUX Detector.

sum to produce the primary scintillation signal (S1), arriving within 10s of ns as the photons are collected the PMT arrays. Electrons which escape recombination with their ion pair feel the effect of the drift field and begin to drift upwards towards the gas phase phase (drift times of 0-324 μs). Once extracted into the gas the electrons accelerate and electroluminece producing a much larger secondary scintillation signal (S2), proportional the the number of electrons extracted. A schematic of an NR and ER event is shown in figure 2.3, figure 2.3 and an illustration of an energy deposition in the LUX detector is show in figure 2.5. The timing separation between the S1 and S2 pulse is used to define the drift time and the hit pattern of the S2 signal on the top PMT array is used to define the XY position of the event. From the S1 and S2 signals the full x,y,z position and energy deposit of the event can be reconstructed.

$$\begin{aligned} \mathrm{E} &= \mathrm{W} \times \mathrm{n_q} + \mathrm{Heat} \\ \mathrm{E} &= \mathrm{W}(\mathrm{n_i} + \mathrm{n_{ex}}) + \mathrm{Heat} \\ \mathrm{E} &= \mathrm{W}(\mathrm{n_\gamma} + \mathrm{n_e}) + \mathrm{Heat} \end{aligned} \tag{2.1}$$

Where E is the energy of the deposit in keV, $\mathrm{n_q}$ is number of quanta (photons + electrons), $\mathrm{n_i}$, $\mathrm{n_{ex}}$, $\mathrm{n_\gamma}$ and $\mathrm{n_e}$ represent the number of ions, exitons, photons and electrons respectively. W for xenon has been measured to be 13.7 $\pm$ 0.2 [quanta/eV] (refs).

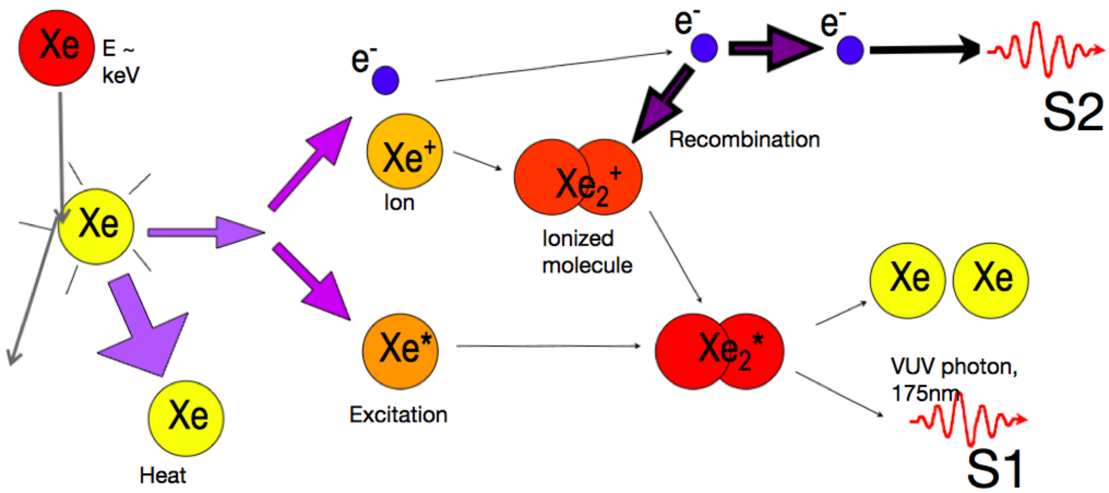

Figure 2.3: Nuclear recoil (NR) event in xenon.

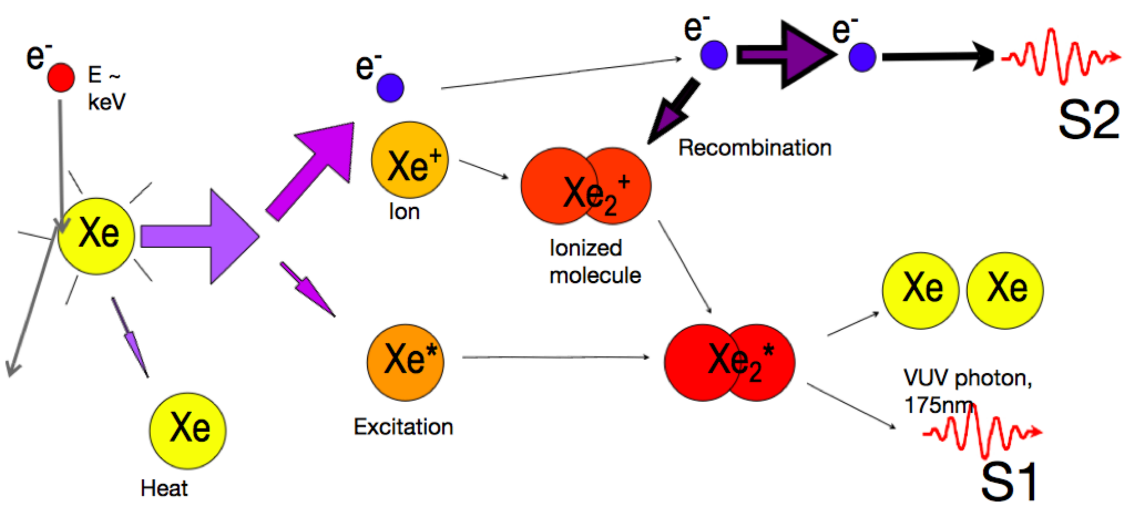

Figure 2.4: Electronic recoil (ER) event in xenon

2.4 Identifying S1, S2

The primary and secondary signals have unique properties which can be used to identify their populations. The S1 signal is a fast spike summed along the PMT arrays, the signal decays in 10s of nano seconds as the primary scintillation and

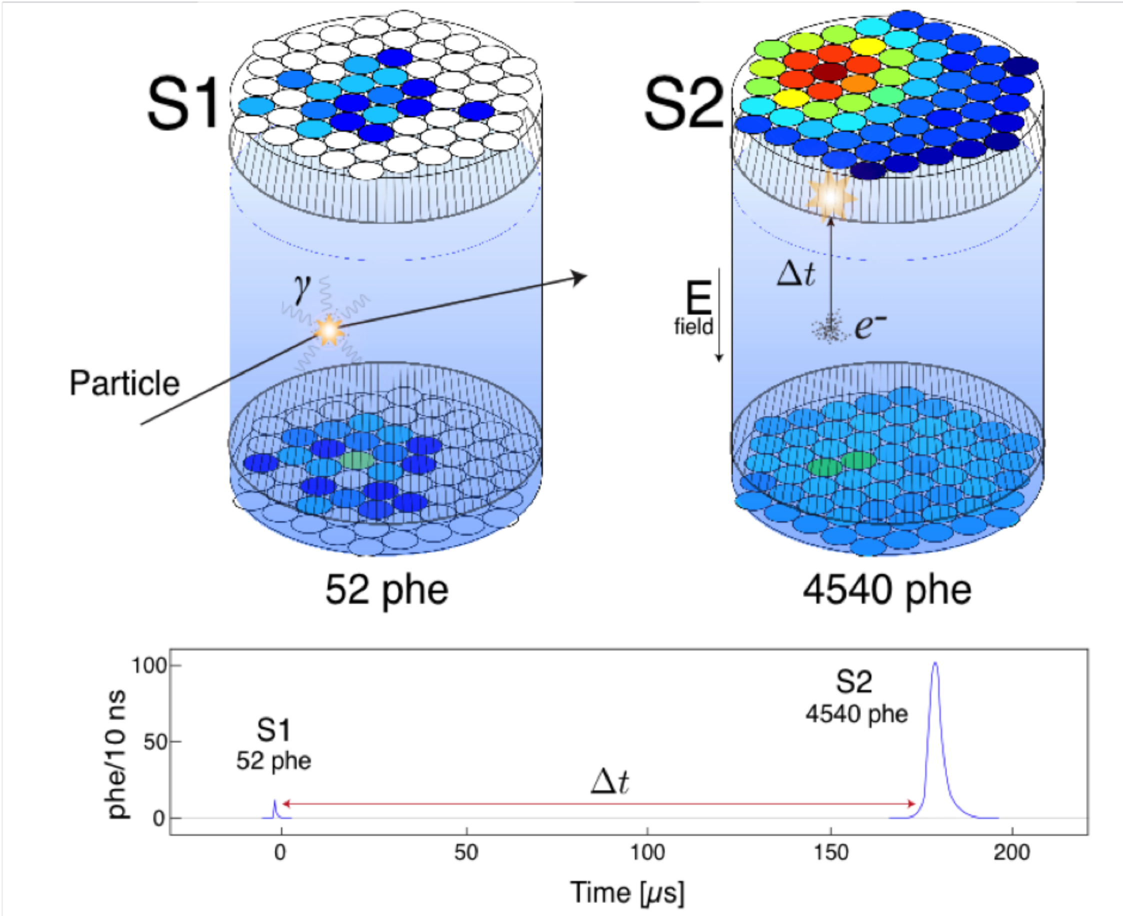

Figure 2.5: Event diagram.

recombining election ion pairs emit photon VUV (175nm). The S2 signal arrives several μs later with the electron population spread out about the centroid of the interaction due to diffusion. The characteristic S2 signal is one with a slow rise and corresponding fall, resembling a bell curve. A 2 keV event as seen by all 122 PMT channels is showing in figure 2.6, the s1 pulse is spiked as the photons arrive and the S2 pulse is much larger with a slower lifetime (the S2 pulse is larger since a single election creates hundred of photons as it is accelerated in the extraction region).

To to the pulse characteristics of S1 and S2 we define a variable Prompt

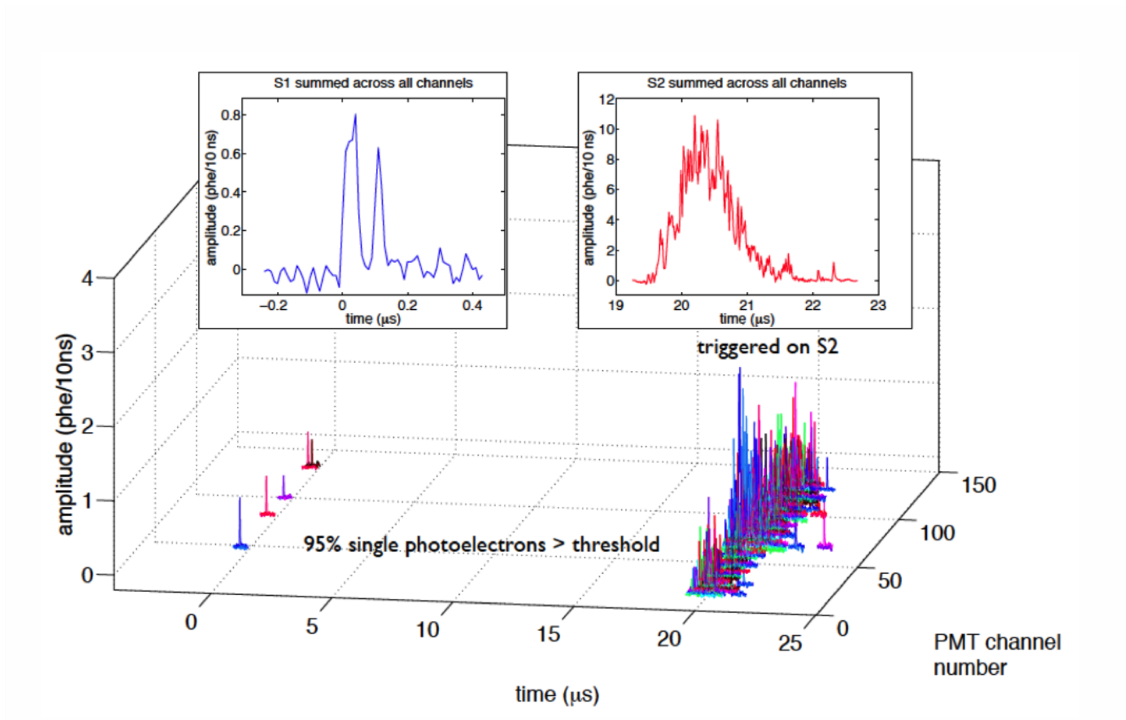

Figure 2.6: LUX 2keV ER event.

Fraction that traces the area covered in the fist 10% of the pulse. For S1s this value will approach 1 and for S2s the value will be below 0.1, this provides for a powerful separation of the populations. The separation of population is shown in figure for the case of a ^{83m}Kr data set (41.5 keV gamma) and a tritium calibration data set (1-18.5 keV beta decay). The populations of single photons, single electrons, S1s and S2s are clearly visible and well separated when plotting the prompt fraction variable vs. pulse area (PE). Figure 2.7 shows the density plot for a ^{83}Kr and Tritium calibration with the population of single electrons, single photons and the S1 S2 pairs associated with gammas, betas and alpha interactions in the LUX detector. We define Golden events for the WIMP search are single scatters with a single S1 paired with a subsequent S2 pulse, with this requirement each golden event has a well defined x,y coordinate and z from the drift time making it possible to correct the signals for geometry and electron attenuation.

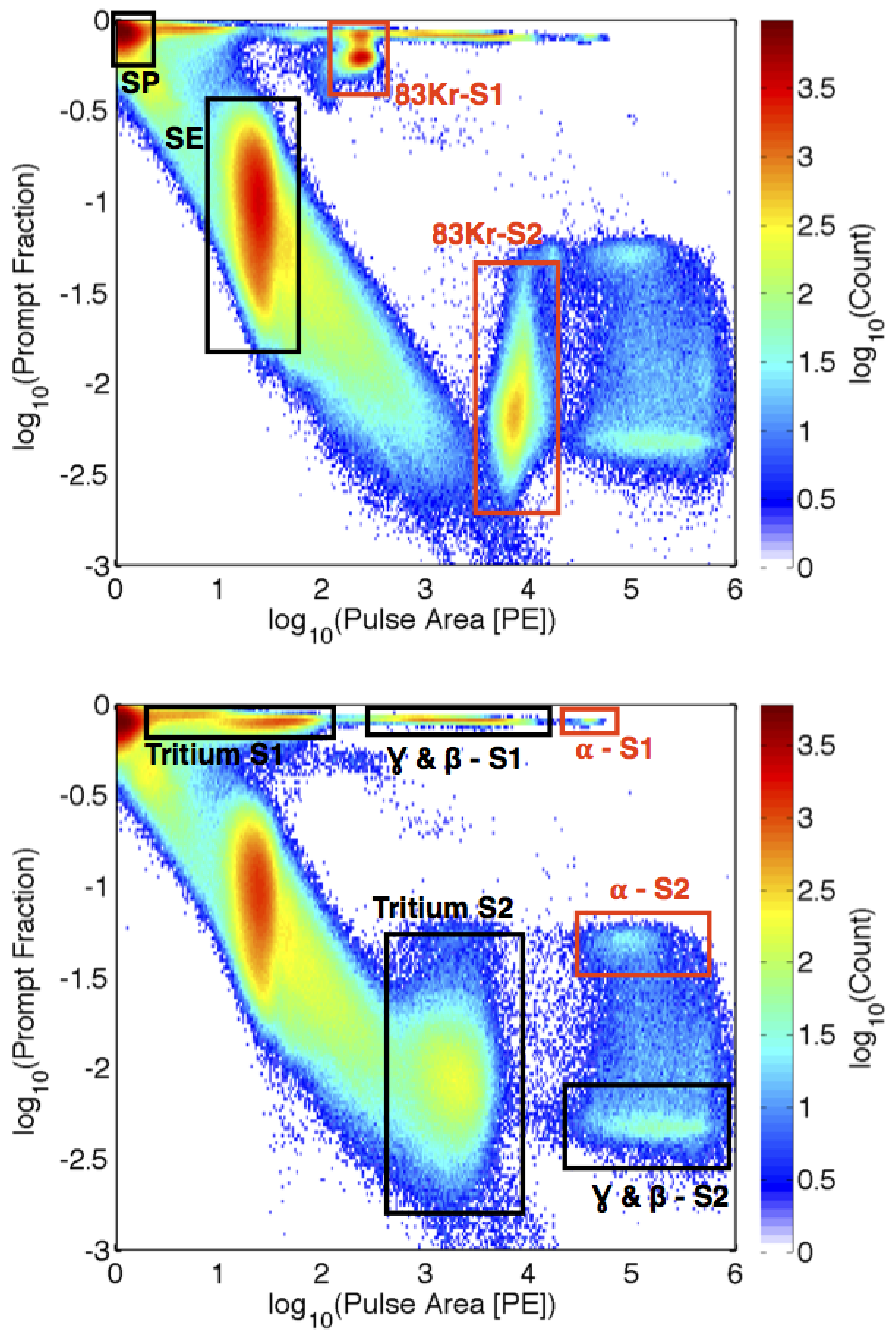

Figure 2.7: Density plot of prompt fraction vs. Pulse Area. Top: ^{83m}Kr data set. Bottom: Tritium data set. Populations of single electrons, single photons and the S1 S2 pairs associated with gammas, betas and alpha are highlighted as rectangles.

Chapter 3: XYZ Correction

3.1 ^{83m}Kr Calibration

Throughout the science run periodic ^{83m}Kr injections were performed to calculate and monitor position dependent corrections. ^{83m}Kr is produced from the decay ^{83}Rb with a half life of 86.2 days, the ^{83}Rb source is housed in charcoal. The daughter 83mKr is continually produced and has a half-life 1.8 hours, ^{83m}Kr first emits a 32.1 [keV] gamma followed by a 9.4 [keV] with a half life of 154 [ns] between the two (refs). The combined signal (41.6 [keV]) is found by the pulse finder in the majority of cases. The ^{83m}Kr source is introduced when needed into the LUX detector by flushing the charcoal housing with xenon along the main circulation path. The ^{83m}Kr source and delivery into the xenon detector is described in more detail in ref[Kastins]. The relatively short half-life of 1.8 hours allows for several injections per week without interrupting WIMP search data taking. Once injected the source is uniformly mixed into the liquid xenon within a matter of minutes and can be used to calculate corrections for the XYZ the response of the detector. Thus, the mono-energetic gamma emitted from ^{83m}Kr is a powerful tool for tracking detector parameters and detector response calibrations over the course of the science run. The better we can flat field the position dependent response to S1 and S2 the lower the observed fluctuations which lead to narrower ER and NR band and ultimately to better signal to background ratio for our WIMP search.

Figure 3.1 shows the distribution of 83mKr events in the LUX detector thirty minutes after the injection.

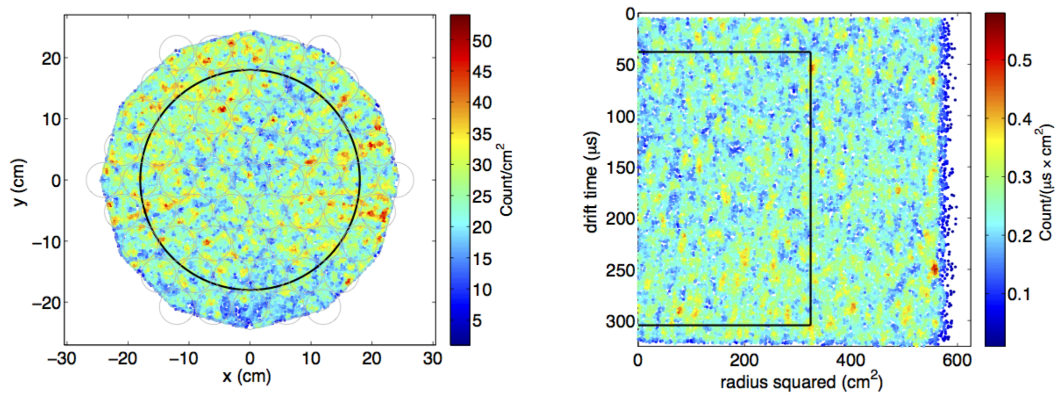

Figure 3.1: Distribution of ^{83m}Kr events 10 minutes after the injection, 50,000 events are shown. The source readily mixed uniformly throughout the liquid xenon illuminating all regions of the active volume. The solid black lines represent the fiducial volume used for the WIMP search.

3.2 S2 Electron Lifetime and x,y Correction

The S1 and S2 signals collected on the top and bottom PMT will have accosted x,y,z positions computed from the S2 hit pattern (x,y) and the signal separation in time (z). Knowing the xyz position provides a powerful tool for reducing fluctuations in the signals due to detector geometry. The dominant effect to correct the data for is the free electron lifetime, as charge is drifted from the event site to the extraction region (0-47 cm) electronegative impurities in the liquid latch onto them. These impurities include residual O_2, H_2O, N_2 in the xenon (1 ppb corresponds to x us [ref]). Through the science run the electron lifetime was measured to be between 500 to 1000 μs (75 to 150 cm drift length), corresponding to between 70% and 50% degradation in S2 signal from the bottom of the detector. The electron lifetime extraction from a ^{83}Kr data set is shown in figure 4. The electron lifetime is calculated by binning the detector in drift time into 60 z slices, in each bin a Gaussian is fit to extract the mean. We then fit an exponential to the mean S2 response vs. z to extract characteristic drift time λ [μs], shown in figure 3.2. For this analysis we use the S2 response on he bottom PMT array, defined as $S2_b$, this convention is chosen since the light in the bottom PMT array is more uniformly distributed than on the top PMTs. Also, two PMTs are not bias on the top PMT arrays which could lead to a significant loss in S2 signal for a potential WIMP events extracted at the location of the unbiassed PMT.

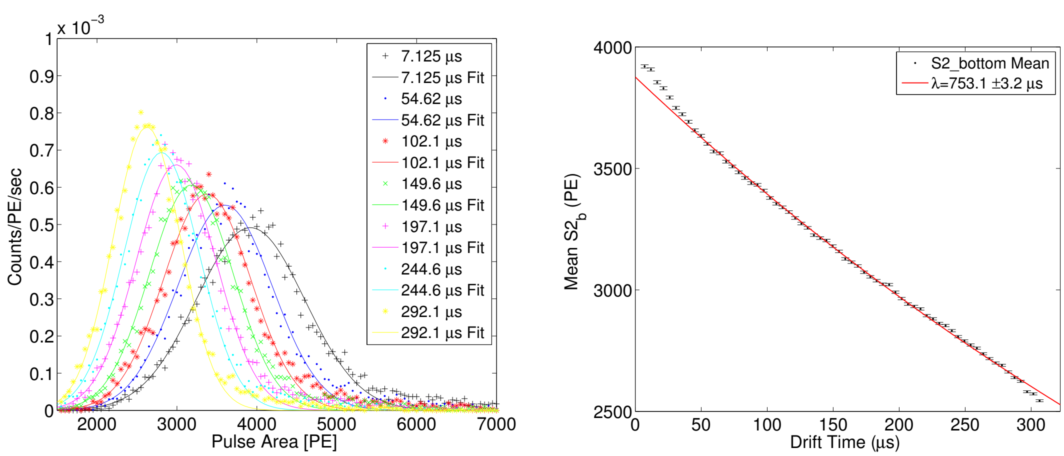

Figure 3.2: Left: Fits to the mean of $S2_b$ in several z slices. Right, the exponential fit to the means of $S2_b$ vs. drift time used to extract electron lifetime λ.

The z corrected $S2_b$ is calculated as follows:

$$S2_{b\text{-}z} = S2_b \cdot \exp\left(\frac{\text{drift time}[\mu s]}{\lambda[\mu s]}\right) \tag{3.1}$$

Where $S2_{b\text{-}z}$ is the z corrected $S2_b$ signal and λ is the free electron lifetime.

After correcting the dominant z dependent electron attenuation, corrected to 0 drift time, we calculate the normalization factor (NF) that will be used to flat field the x,y dependance of the S2 signal. The S2 light is emitted when the charge is extracted from the liquid above the gate and is accelerated through 6 kV and traversing 5mm to the anode. Fluctuations in XY response to a given number of electrons are caused by non uniformities in the extraction field, tilt in the liquid level, and non uniformities in the anode-gate separation (potentially wire sagging). All these variations lead to additional fluctuations in the S2 signal, but by using a the ^{83m}Kr the response can be corrected as a function of x,y position. The normalization is calculated by creating a 25x25 grid on the XY plane, corresponding to 2[cm] x 2[cm] x,y bins, for each bin center the average light response is determined by fitting a Gaussian. Figure 3.3 on the left, shows the measured $S2_b$ response to 1 million ^{83m}Kr decays normalized to the response at the center, x=y=0, this map represents the inverse of the normalization to the center that we call NF(x,y). NF is then applied to the $S2_b$ data by using a spline interpolation of the x,y coordinate of each event relative to the bin centers NF(x,y). Figure 3.3 on the right, shows the $S2_b$ response after flat fielding the data relative to the center x=y=0 using NF(x,y). After applying the x,y correction the fluctuation decrease from 10% to 1% in the inner 18 cm of the detector (the fiducial volume).

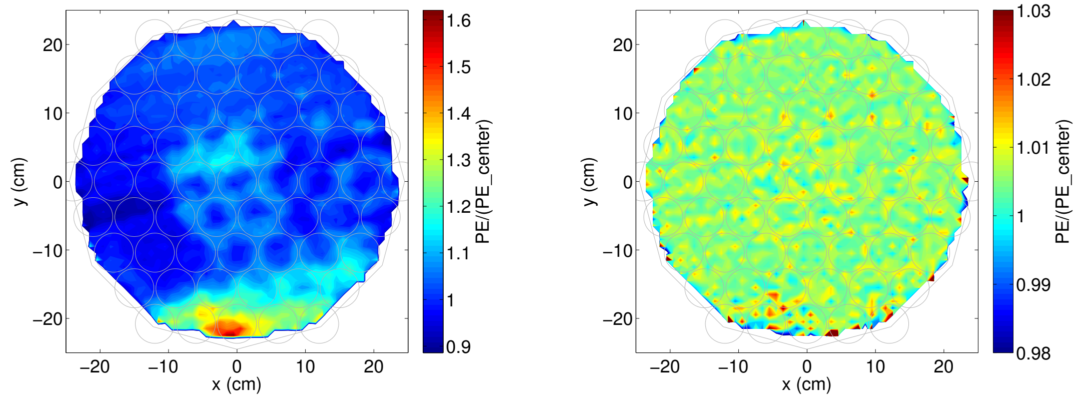

Figure 3.3: $S2_b$ XY Correction.

After correcting for z and x,y we can define the position dependent (x,y,z) corrected $S2_b$ signal, which we will call $S2_{bc}$ calculated as follows:

$$S2_{\text{b-c}} = S2_{\text{b-(x,z,y)}} = S2_{\text{b-z}} \cdot \mathcal{NF}_{S2_b}(x, y) \tag{3.2}$$

Where $S2_{\text{b-c}}$ is the x,y,z corrected $S2_b$ signal and $NF_{S2_b}(x, y)$ is the 'Normalization Factor' of the bottom PMT array for S2s and is a function of x,y. The interpolation of the inverse of $NF_{S2_b}(x, y)$ along the x,y grid is plotted in figure 3.3.

After applying the z correction to $S2_b$ there is an improvement in resolution of 18%, for the case of an 750 μs electron lifetime. The flat fielding in the x,y plane provides an additional 4.9% improvement in resolution to the $S2_b$ signal. Figure 3.4 shows the improvement in the $S2_b$ signal after applying the z and x,y correction.

3.3 S1 x,y,z Correction

The S1 light is emitted from the interaction sight, unlike the S2, and has about a 30% variation in light collection efficiency between events near the top and bot-

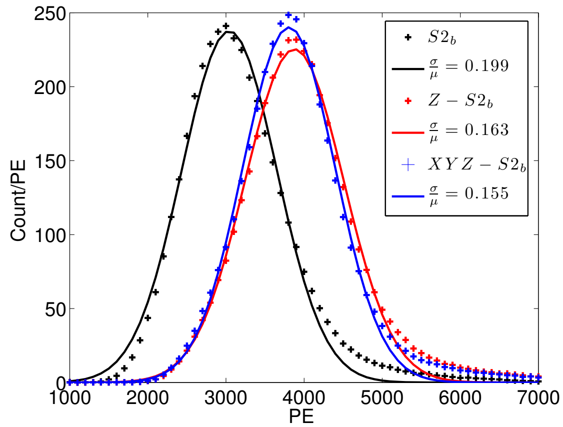

Figure 3.4: Improvement of resolution in $S2_b$ after applying the z and x,y,z correction.

tom of the detector. About 2/3 of the S1 light is collected on the bottom PMT arrays due to total internal reflection at the liquid gas interface near the top of the detector, and as events move closer to the bottom PMTs the probability of a photon sticking a PMT and producing a photo electron (PE) increases. Other position dependent effects include the photon absorption length which is negligible at the purities achieved in LUX and teflon reflectivity, about 95%. Any quantum efficiency (QE) variations between the 122 PMTs that are not corrected out by the individual gain corrections are also folded into the S1 position dependent correction derived from the ^{83m}Kr calibrations. To calculate the x,y,z dependent Normalization Factor for S1 (NF_{S1}) the detector is divided into a 25x25x16 x,y,z mesh with each voxel having dimensions of 2[cm] x 2[cm] x 20[μs]. To achieve sufficient statistics for flat fielding we require at least 400,000 ^{83m}Kr events, giving about 40 events per voxel to define the mean. However, we have monthly high stats calibrations that produce 1 million counts providing our NF correction maps. Unlike the S2 correction, which is highly dependent on purity the S1 has been found to be invariant to within a percent over the course of the science run, thus monthly calibrations with high stats are sufficient to provide the position dependent correction.

Figure 3.7 shows the response of the detector to ^{83m}Kr normalized to the center of the detector in 16 slices of z each and a 2[cm] x 2[cm] x,y grid. The plotted maps and normalized to the center of the detector and represent the inverse of the normalization factor ($\mathrm{NF_{S1}}$). We choose to normalize the the center of the detector as it represents the overall average light collection efficiency of the detector as this value varies roughly linearly from top to bottom, with lower light collection at the top and higher light collection at the bottom. Though the dominate correction is the z dependance there is also substructure to each z slice in x,y which is showing in figure 3.6, where we have normalized each slice to its own center. We can see that near the top and bottom we pick up additional geometric effects from being near the edges, whereas in the central z slices the uniformity is much greats due to increased scattering off the teflon.

We define the position dependent (x,y,z) corrected S1 signal as $\mathrm{S1_c}$, normalized to the center of the detector (x=y=0 and z=160μs) calculated as follows:

$$\mathrm{S1_c = S1_{(x,z,y)} = S1 \cdot \mathcal{NF}_{S1}(x, y, z)} \tag{3.3}$$

Where $\mathrm{S1_c}$ is the x,y,z corrected S1 signal and $\mathcal{NF}_{\mathrm{S1}}(\mathrm{x, y, z})$ is the Normalization Factor of the sum of all PMTs for S1s and is a function of x,y,z. The interpolation of the inverse of $\mathrm{NF_{S1}(x, y, z)}$ along the x,y grid in z slices is plotted in figure 3.7. The normalization factor is applied to the S1 data by using a

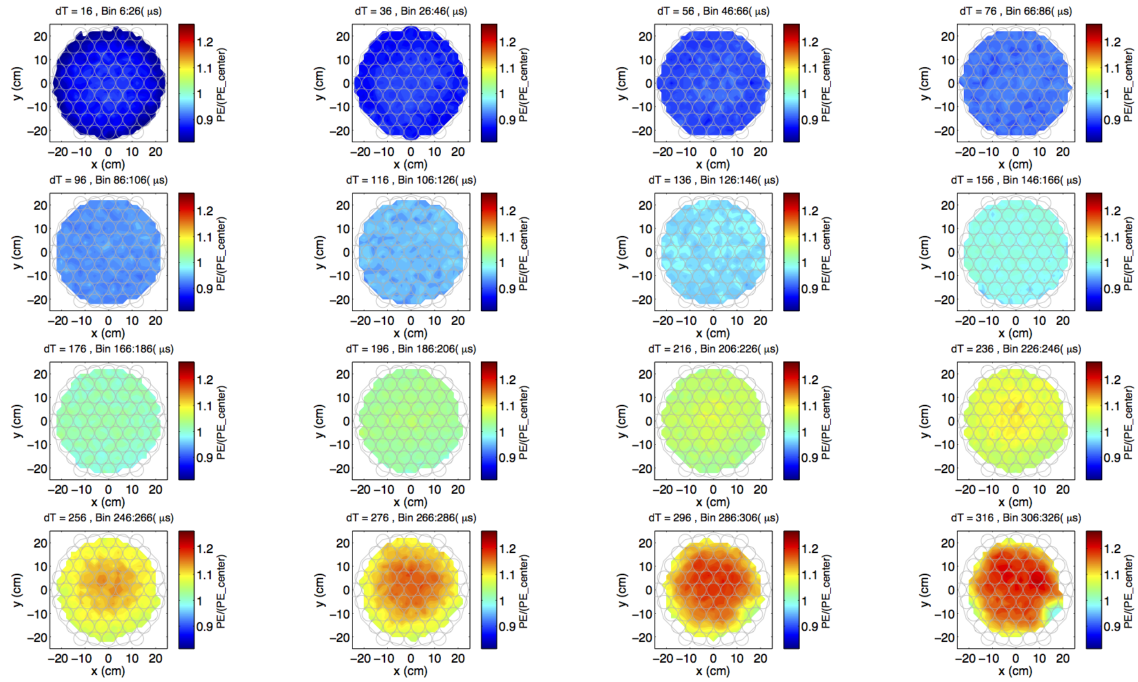

Figure 3.5: S1 x,y,z response normalized to the center of the detector. The interpolated map represents the inverse of the normalization factor $\mathcal{NF}$.

spline interpolation of the x,y,z coordinate of each event relative to the bin centers $\mathcal{NF}_{\mathrm{S1}}(\mathrm{x},\mathrm{z},\mathrm{y})$. Figure 3.7 shows the S1 response after flat fielding the data relative to the center of the detector. After applying the x,y,z correction the position dependent fluctuations decrease to less than1% in the inner 18 cm of the detector (the fiducial volume), with as much as 3% fluctuations near the top and bottom edges were the interpolation breaks down.

After applying the z correction to S1 there is an improvement in resolution of 31.5%. The flat fielding in z and the x,y plane provides an additional 2.0% improvement in resolution in S1 over the z only correction. Figure 3.8 shows the improvement in the S1 signal after applying the z and x,y,z correction.

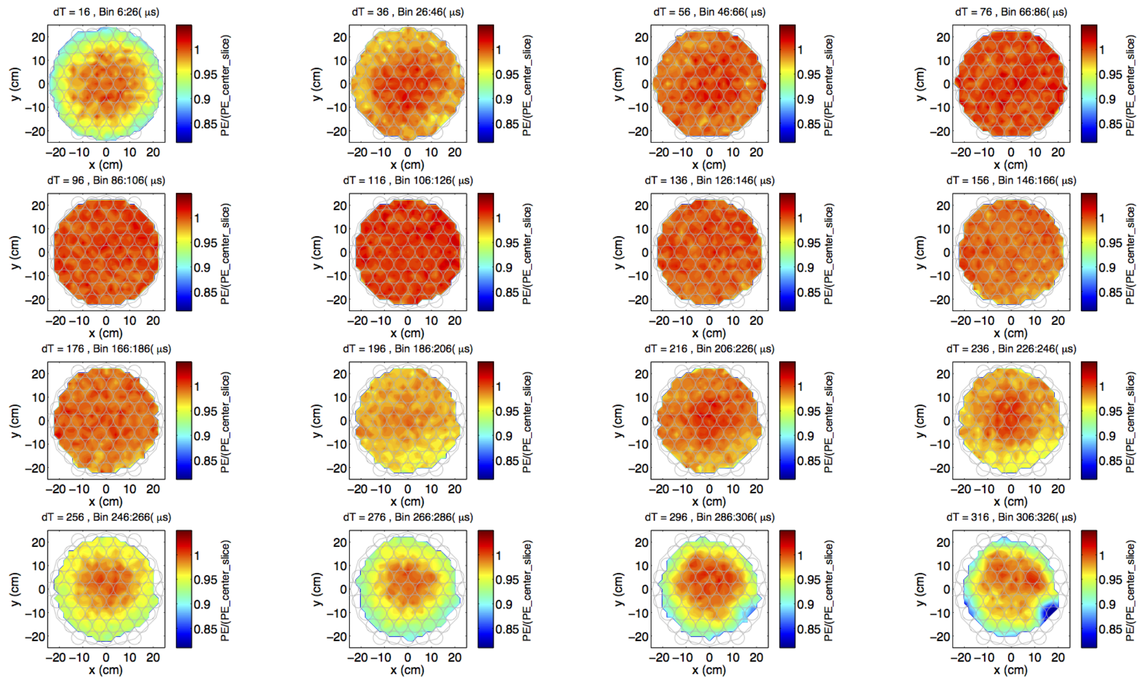

Figure 3.6: S1 x,y,z response normalized to the center of each z slice. We see significantly more variation near the very top and bottom 4 z slices as the solid angle for light hitting the PMT arrays are increased. For the central slices the x,y response is uniform due to increased scattering off the teflon panels before light strikes one of the PMT arrays.

3.4 Application to x,y,z Corrections in Data Processing

As mentioned earlier, the purpose of the periodic ^{83m}Kr calibrations were to produce position dependent S1 and S2 corrections over the corse of the science run. Before processing the WIMP search data the calibration sets were processed and a MYSQL table of electron lifetimes and corrections maps were populated for each date. The electron lifetime applied to each WIMP search data set was a linear interpolation between calibration dates, for the x,y correction the nearest $\mathcal{NF}_{\mathrm{S2}}(\mathrm{x,y})$ entry in

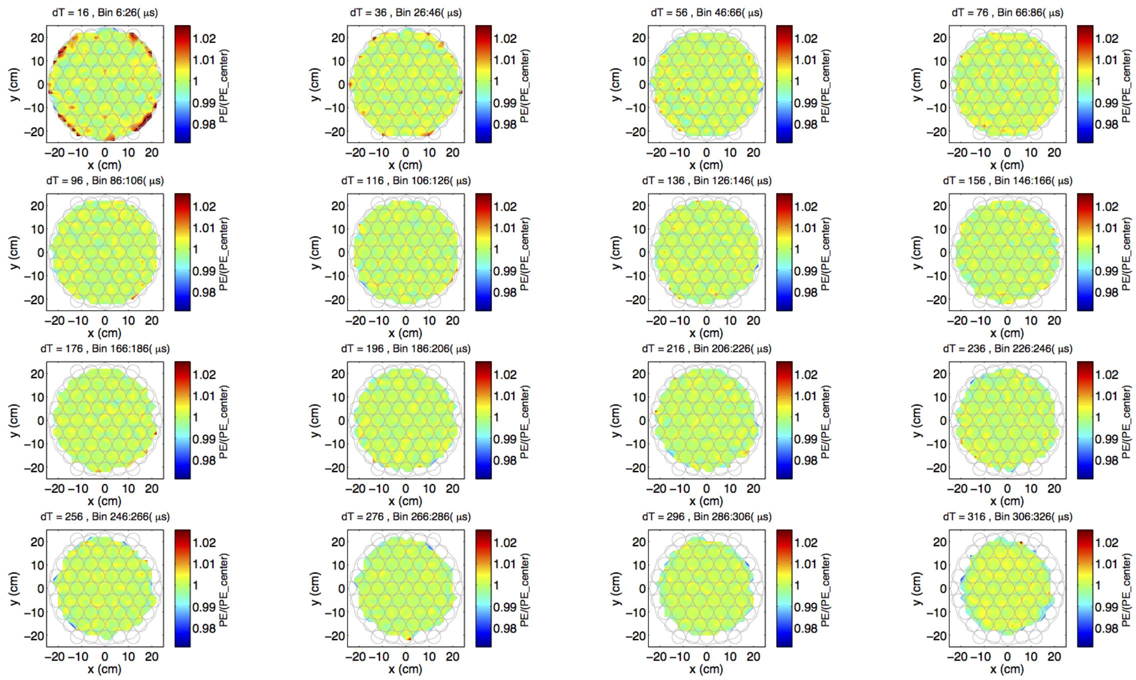

Figure 3.7: S1 x,y,z response normalized to the center of the detector after the data has been flat fielded and normalized to the detector center. The remaining fluctuations in the fiducial volumes (r<18cm) are less than 1%, near the top and bottom edges the deviation increases to as much as 3% due to the interpolation of the correction breaking down.

time was used. Combined these produced the corrected $S2_c$ quantity to be used for the WIMP analysis. For the S1 x,y,z corrections the nearest $\mathcal{NF}_{S1}(x, y, z)$ entry was used to produced the corrected $S1_c$ quantity. For both the S2-x,y and S1-x,y,z correction the time dependance is assumed to be neglidgable as these are geometric effects, whereas the electron lifetime varies with purity daily. The electron lifetime and the stability of the z dependent S1 correction over the corse of the first science run is shown in figure 3.9 and 3.10. While the electron lifetime needs frequent monitoring the S1 x,y,z response is fixed over several months of running. For the

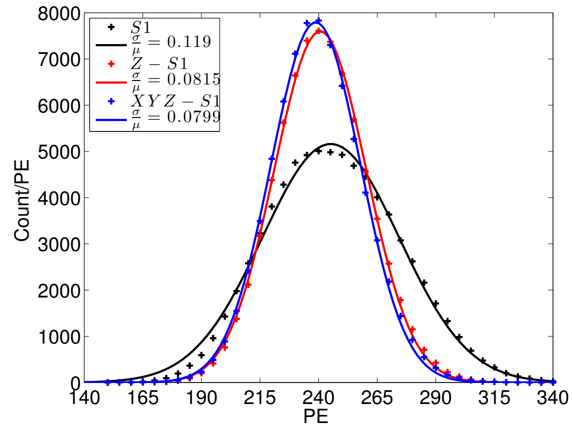

Figure 3.8: Improvement of resolution in S1 after applying the z and x,y,z correction.

results discussed in the subsequent sections of the thesis we will only work with the x,y,z corrected S1 and $S2_b$ pulses defined at $S1_c$ and $S2_{bc}$ respectively.

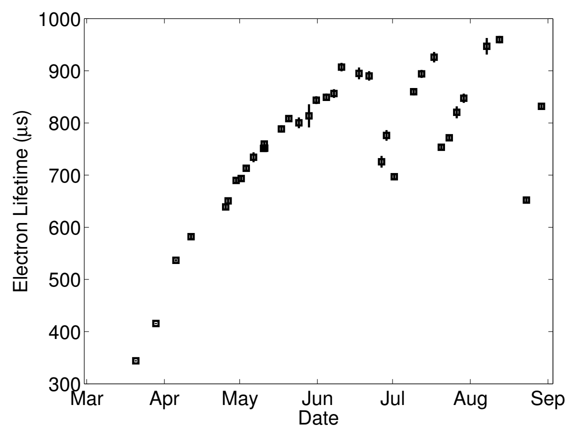

Figure 3.9: Electron lifetime measured using periodic ^{83m}Kr calibrations over the corse of the LUX science run in 2013.

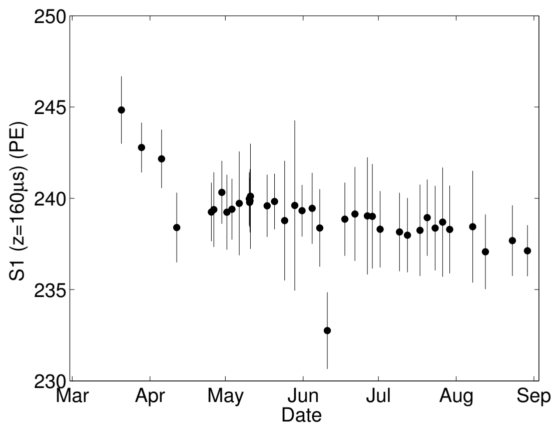

Figure 3.10: Measured response of to light from ^{83m}Kr calibrations at the center of the LUX detector over the corse of the LUX science run in 2013.

Chapter 4: Energy Scale Calibration

4.1 Calibrating the Combined Energy Scale

This section outlines the method used to calibrate the energy scale of the dual phase LUX detector. The idea behind the method is to take calibration data with multiple sources and/or electric fields and combine the measured scintillation signals, primary (S1) and secondary (S2) in order to reconstruct energy. For a given energy deposit in liquid xenon an amount of quanta released is proportional to a work function W, for nuclear recoils we must also consider heat loss. The quanta created at the interaction site are the results of electron-ion pairs and exitons produced by the recoiling xenon nucleus, equation 4.1. Exitons quickly de-excite and contribute to the primary scintillation signal (S1). Ions that recombine with their electron pairs produce scintillation light (S1), while those electrons that do not recombine are collected several μs later in the extraction region as the larger secondary scintillation signal S2. There are two knobs to turn that tune the recombination fraction and probe combined energy space over a variety of S1 and S2, we can either change the energy of the source or adjust the drift field. The larger the spread in S1 and S2 the more constrained the combined energy scale will be. Measuring both light and charge allows for a vastly improved resolution compared with only using a single S1 or S2 only space, since recombination fluctuations cancel out if energy is reconstructed correctly.

$$
\begin{aligned}
\mathrm{E} &= \mathrm{W}(\mathrm{n_i} + \mathrm{n_{ex}}) \\
\mathrm{E} &= \mathrm{W}(\mathrm{n}_\gamma + \mathrm{n_e})
\end{aligned}
\tag{4.1}
$$

Using equation 4.1 and assuming that the heat loss is negligible for electronic recoils (ER) we can reconstruct energy by knowing the work function and the conversion from measured S1(light) and S2(charge) signals to the number of quanta ($\mathrm{n}_\gamma + \mathrm{n_e}$) liberated by the interaction. We define gain-1 (g1) and gain-2 (g2) as the conversion from initial number of photons and electrons propagated from the interaction site to the observed signal by the PMT arrays as a photo electron (PE), given in equation 4.2. By using multiple mono energetic sources with know energies we can extract a best fit for the value of the gains (g1,g2) by making a Doke plot [ref]. The mono energetic lines used for the purposes of the calibration are listed in table 4.1. For each calibration point we plot the mean S1/E vs. mean S2/E (Equation 4.3) and fit a line, the x and y intercepts (Equation 4.4) yields the value of g1/W and g2/W respectively. The value of the work function W in liquid xenon has been found to be 0.0137 ± 0.002 [quanta/keV] [ref]. The values of g1,g2 are degenerate and highly correlated such that the ratio of g1:g2 is always a constant, a reduction in g1 can be compensated by an increase in g2 and still yield the same number of initial quanta and visa versa. Breaking the degeneracy requires data over a wide range of S1 and S2 values near the intercept of the Doke plot. Due to the strong correlation in the fit parameters the data is fit by minimizing the likelihood and the errors in intercept and slope are determined using MCMC (Markov Chain Monte Carlo).

$$\begin{aligned}\langle \mathrm{n}_\gamma \rangle &= \frac{\langle \mathrm{S1} \rangle}{\mathrm{g}_1} \\ \langle \mathrm{n}_\mathrm{e} \rangle &= \frac{\langle \mathrm{S2} \rangle}{\mathrm{g}_2}\end{aligned} \tag{4.2}$$

$$\begin{aligned}\mathrm{S1/E} &= \frac{\mathrm{n}_\gamma}{(\mathrm{n}_\gamma + \mathrm{n}_\mathrm{e})} \times \frac{\mathrm{g1}}{\mathrm{W}} \\ \mathrm{S2/E} &= \frac{\mathrm{n}_\mathrm{e}}{(\mathrm{n}_\gamma + \mathrm{n}_\mathrm{e})} \times \frac{\mathrm{g2}}{\mathrm{W}}\end{aligned} \tag{4.3}$$

$$\begin{aligned}1 &= \left(\frac{\mathrm{S1}}{\mathrm{E}}\right)\left(\frac{\mathrm{W}}{\mathrm{g1}}\right) + \left(\frac{\mathrm{S2}}{\mathrm{E}}\right)\left(\frac{\mathrm{W}}{\mathrm{g2}}\right) \\ \left(\frac{\mathrm{S1}}{\mathrm{E}}\right) &= \left(\frac{\mathrm{g1}}{\mathrm{W}}\right) - \left(\frac{\mathrm{S2}}{\mathrm{E}}\right)\left(\frac{\mathrm{g1}}{\mathrm{g2}}\right) \\ \mathrm{y} &= \frac{\mathrm{S1}}{\mathrm{E}}, \mathrm{x} = \frac{\mathrm{S2}}{\mathrm{E}}, \mathrm{y} = \mathrm{m} \cdot \mathrm{x} + \mathrm{b} \\ \mathrm{g1} &= \mathrm{b} \cdot \mathrm{W} \\ \mathrm{g2} &= \frac{\mathrm{g1}}{\mathrm{m}} = \frac{\mathrm{b} \cdot \mathrm{W}}{\mathrm{m}}\end{aligned} \tag{4.4}$$

4.1.1 Anti-Correlation Space

The first step in calibrating the energy scale is to plot the observables S1 vs. S2, by doing this the anti correlation between light and change at a given energy become apparent, figure 4.1. For the data presented here a fiducial cut was placed at a radius of less than 18 [cm] and drift distance between 6 and 46 [cm] which greatly reduces

Source	Energy [keV]	Decay Type
Xe K shell	29.7, 34	X-ray
^{83m}Kr	41.55**	Internal Conversion
^{131}Xe	163.9	Internal Conversion
^{127}Xe	203 or 375	^{127}I daughter γ-emission
	33.8	Kb shell X-ray
	5.3	L shell X-ray
^{129m}Xe	236.1	Internal Conversion
^{214}Bi	609	γ-emission
^{137}Cs	661.6	Photo-absorption

Table 4.1: Mono energetic peaks used for g1 g2 calibration. ** Kr83 data was taken at 50 and 105 [V/cm] along with the standard field of 180 [V/cm].

the background event rate. To extract g1 g2 we first determine the average values of S1 and S2 at each known energy. Initially loose diagonal cuts are placed by eye on the populations, figure 4.1. Next, using a un-binned maximum likelihood fit the mean and sigma are estimated and then refit using $\pm 2\sigma$ of the initial distribution to remove tails from backgrounds. With the initial estimate for the mean S1 and S2 response to a given energy the gains g1,g2 are determined. The resulting value of g1 and g2 is found to be 0.096 ± 0.009 and 5.94 ± 1.68 respectively, the fit is shown in figure 4.2. The values of g1 and g2 represent a best fit tot he underling recombination theory where for each additional photon there is a corresponding reduction of one electron and visa versa. The method for extracting the uncertainties using MCMC will be discussed later in section 4.1.3.

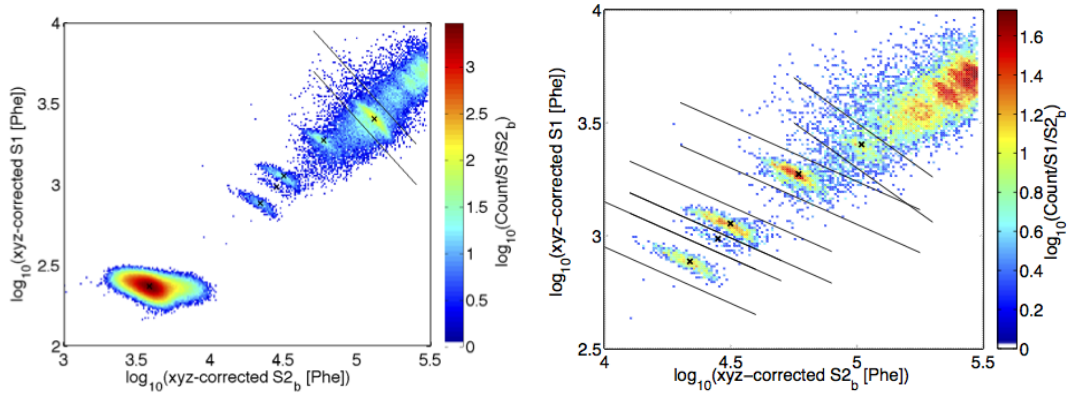

Figure 4.1: LUX data in anti correlation space (S1 vs. S2), the black lines indicate the initial cuts by eye used to isolate populations of constant energy. In both figures diagonals represent lines of constant energy with a slope depending on the local recombination probability. The centroids found by an unbind maximum likelihood analysis are shows as a black X, for sources show in table 4.1.

4.1.2 Refitting in Combined Energy Space

From the first attempt to find g1,g2 we see, in figure 4.2, that there are discrepancies between the data and the fit, however this first result is only a crude estimate derived from anti correlation space. Once we have an initial estimate of gains g1,g2 a combined energy scale can be constructed with significantly improved resolution over the initial guess, due to the fact that recombination fluctuations are canceled. With the improved resolution the data are fit around the combined energy peaks using an unbinned maximum likelihood fit to a normal distribution, and then the data refitted around 1.5 σ of the initial fit. The fits used to extract the means and sigmas of the S1 and S2 signals at a given energy are show in figures 4.4 and

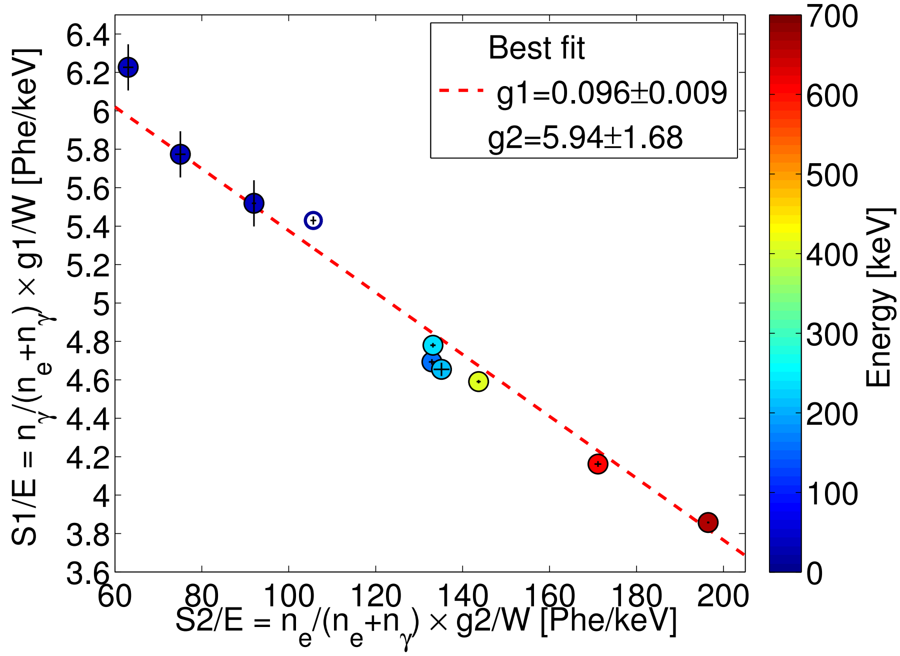

Figure 4.2: Doke plot showing the best fit for the energy calibration parameters g1 and g2 using S1 and S2 means extracted from anti-correlation space. The first three blue points, from the left, are from ^{83}Kr calibrations at 50, 105 and 180 V/cm respectively. The open circle was from the K-shell xenon X-ray and was not used for the fit as it's absolute energy and origin from the skin of the detector is uncertain.

4.5. We iterate this technique twice as the convergence is rapid, in this case the initial value of g1 and g2 derived from anti-correlation space are already a close approximation to the true value. The resulting value of g1 and g2 is found to be 0.097±0.008 and 5.75±1.4 respectively, the fit is shown in figure 4.3. After refitting there is a significant improvement over figure 4.2, especially the xenon activation lines in the center, which is due to better peak finding in combined energy space over anti-correlation space.

$$g1 = 0.097 \pm 0.008$$
$$g2 = 5.75 \pm 1.4 \tag{4.5}$$

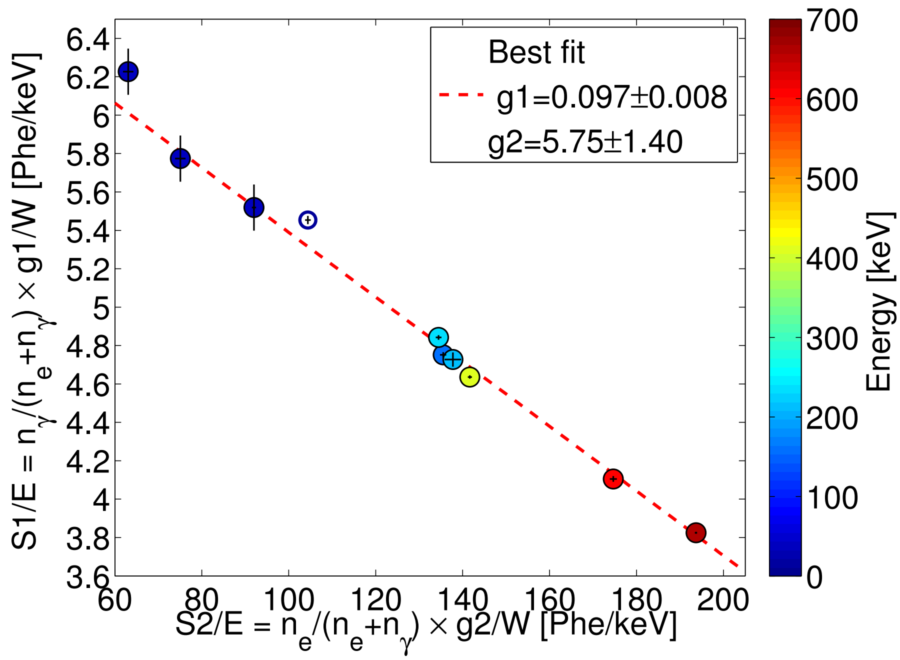

Figure 4.3: Doke plot showing the best fit for the energy calibration parameters g1 and g2 using S1 and S2 extracted from a combined energy space. The first three blue points, from the left, are from ^{83}Kr calibrations at 50, 105 and 180 V/cm respectively. The open circle was from the K-shell xenon X-ray and was not used for the fit as it's absolute energy and origin from the skin of the detector is uncertain.

Figure 4.6 is the final Doke plot for multiple peaks the theory describes the data well using the optimal fit for g1 and g2, for each increase in number of photons there is a corresponding decrease in the number of electrons and visa versa. The relatively large error on g2 is due to the distance of the data points from the x-intercept. As stated before the values of g1 and g2 can be locally degenerate as long

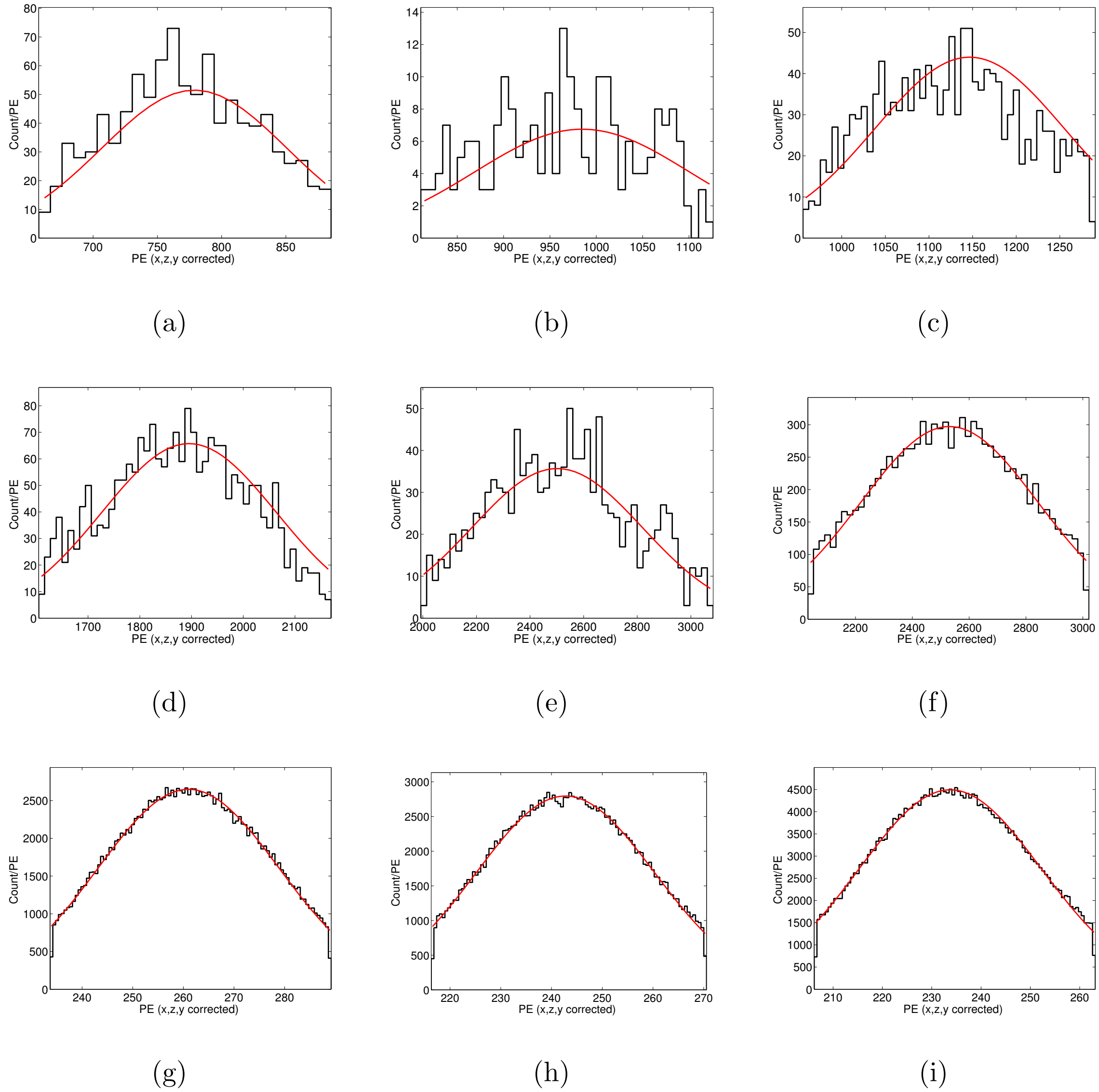

Figure 4.4: S1 fits to sources at nominal field of 180 [V/cm] unless otherwise noted. Source and energy in keV from top left to bottom right: a) ^{131}Xe: 163, b) ^{127}Xe: 207, c) ^{127}Xe & ^{129m}Xe: 236.8, d) ^{127}Xe: 410, e) ^{214}Bi: 609, f) ^{137}Cs: 661.6, g) ^{83m}Kr: 41.5 - at 50 [V/cm], h) ^{83m}Kr 41.5 - at 105 [V/cm], i) ^{83m}Kr 41.5 .

as their ratio remains a constant. Thus for future studies it will be important to probe more of the parameter space in order to place a tighter constraint on gains g1 and g2.

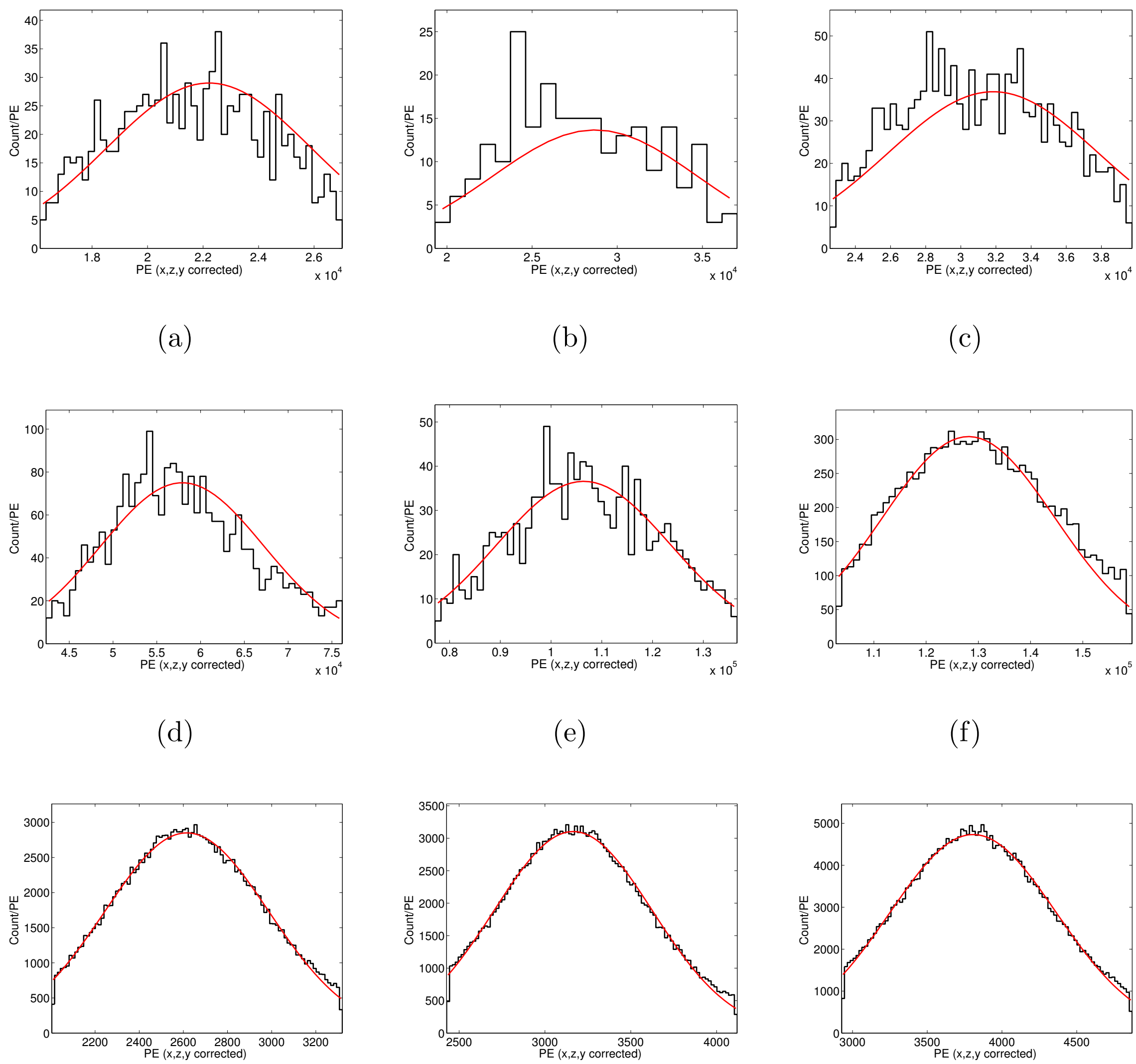

(a) (b) (c)

(d) (e) (f)

(g) (h) (i)

Figure 4.5: S2 fits to sources at nominal field of 180 [V/cm] unless otherwise noted. Source and energy in keV from top left to bottom right: a) ^{131}Xe: 163, b) ^{127}Xe: 207, c) ^{127}Xe & ^{129m}Xe: 236.8, d) ^{127}Xe: 410, e) ^{214}Bi: 609, f) ^{137}Cs: 661.6, g) ^{83m}Kr: 41.5 - at 50 [V/cm], h) ^{83m}Kr 41.5 - at 105 [V/cm], i) ^{83m}Kr 41.5 .

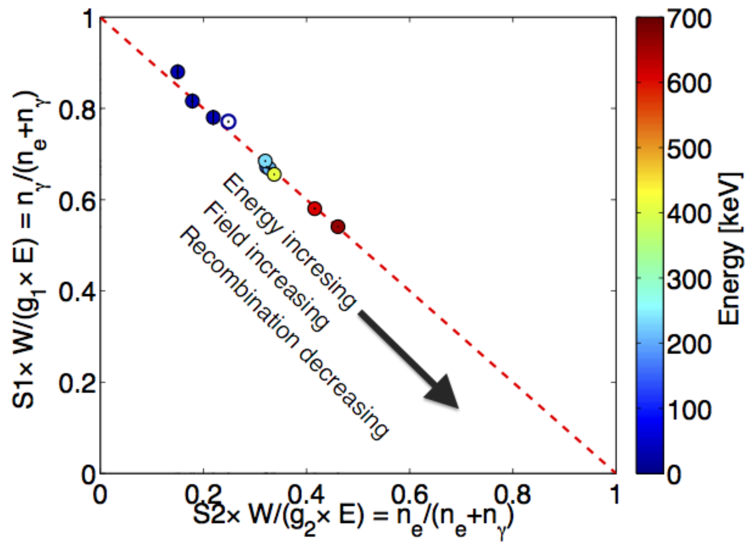

Figure 4.6: Doke plot of the data showing the light yield vs. charge yield. Only solid circles are used for the fit, the open circle is the Xe K shell X-ray from the detector edge.

4.1.3 Finding Errors with MCMC

The error bars reported in this section on g1 and g2 are from the error in the slope and intercept of the linear fit in the Doke plot derived using MCMC. For calculating the error in slope and intercept three random walkers were used at each data point and allowed to take 500 steps.The MCMC takes into account the covariance of the parameters, shown in figure 4.7 as a two dimensional Gaussian. There is a strong negative correlation between the slope m and intercept b which is the result of the degeneracy between gains g1 and g2 used to reconstruct energy by combining the light and charge signal. Thus, the error on g1 and g2 is such that for the positive maxima deviation in g1 we reach the negative maxima of the error on g2, and visa versa. Using standard reduced χ^2 for fitting and calculating errors in the slope and intercept would be underestimated the true error by a factor of five as it does not account for the degeneracy of the anti-correlated gains.

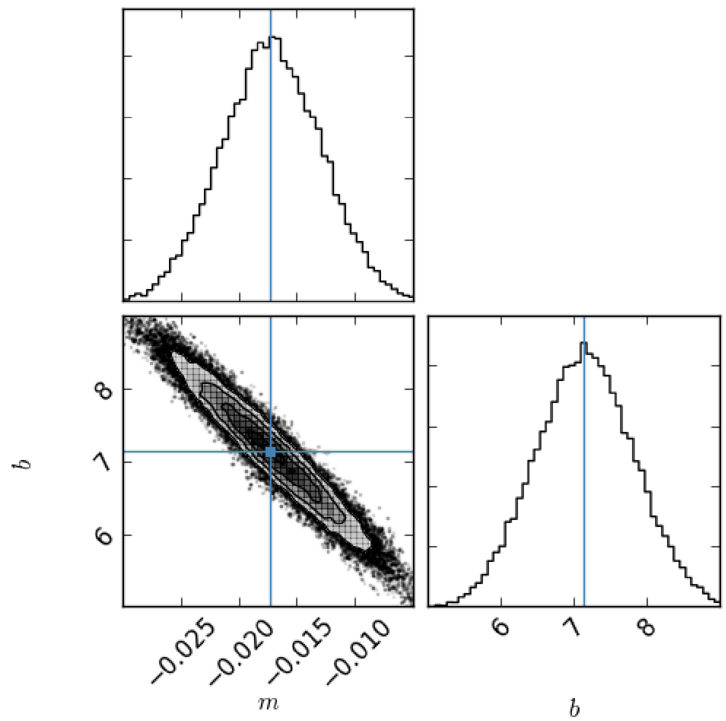

Figure 4.7: MCMC for the linear fit to the Doke plot. There is a strong negative correlation between the slope m and intercept b which results from the degeneracy between gains g1 and g2.

4.1.4 Combined Energy Space

With the values of g1 and g2 known the combined energy of events can be reconstructed with a significant improvement over using only the light or charge channel. In combined energy space recombination fluctuations are removed by the anti correlation of light and charge production and any residual smearing is due to intrinsic detector resolution (discussed later in section :) . Figure 4.8 shows the energy histograms of the data used for the fits to gains g1 and g2 including the xenon activation lines and the ^{137}Cs calibration, along with a zoom in of the xenon K shell Xray at 34 keV and a 81 keV gamma from ^{133}Xe, not used for finding g1,g2. With the energy scale calibrated we can now reconstruct the energy of the events and convert the measured S1 and S2 signals to fundamental quanta using the gains g1,g2 allowing us to untangle instrumental and recombination fluctuations and measure light and charge yields.

4.1.5 Light Collection and Electron extraction

The value of g1 represents the mean efficiency for collecting photons at the center of the LUX detector, the response to S1 light is flat fielded and normalized to the detector center (section Kr calibrations). The measured value of g1= 0.097 ± 0.008 implies a 9.7% probability of a photon propagated from the center of the detector stricking a PMT and being converting into a photo electron (PE) signal. The value of g2 represents the average number of PE collected for each electron that escaped recombination at the initial interaction site and then drifted,by the electric field,

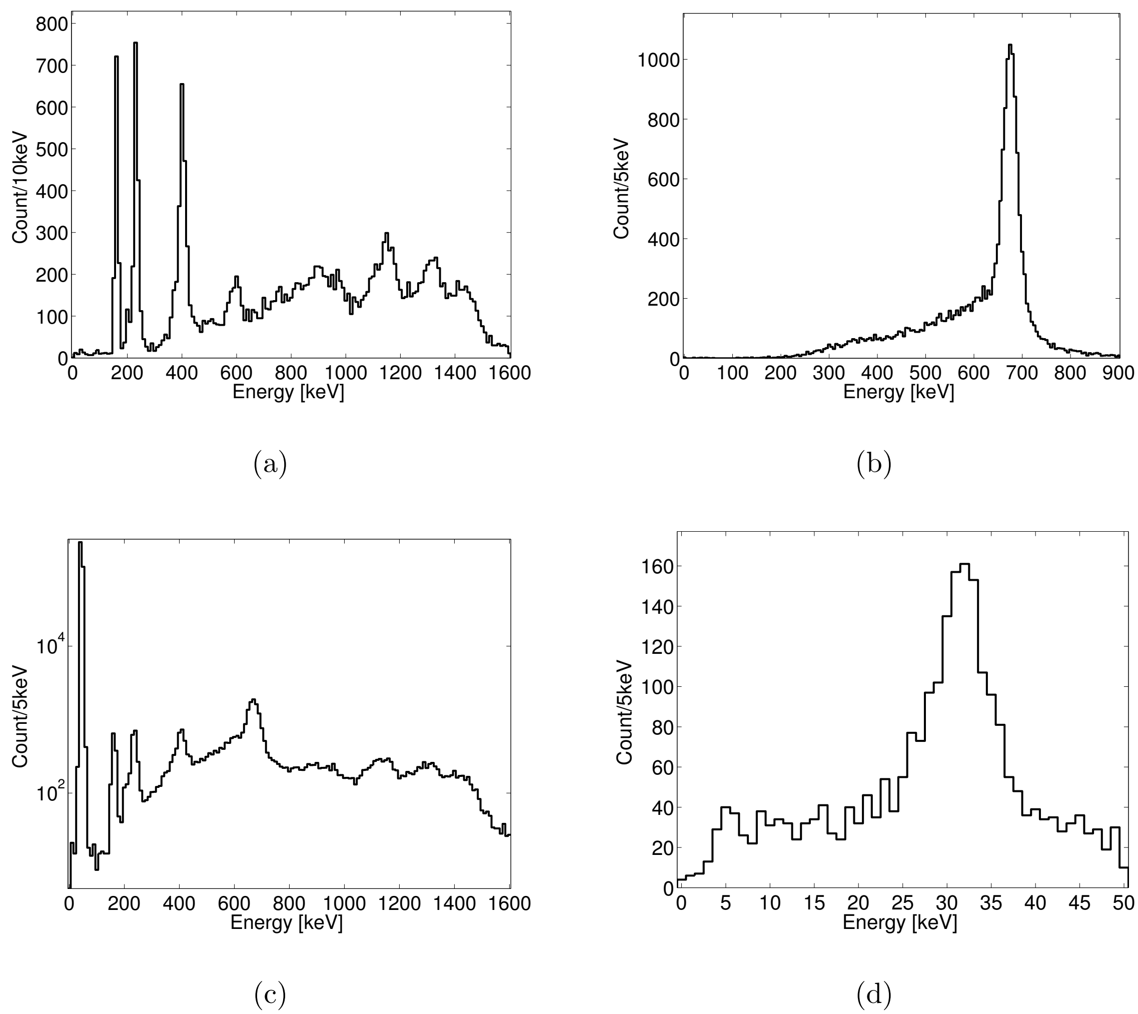

Figure 4.8: Combined energy scale. a) The xenon activation lines from early in the run. b) ^{137}Cs calibration data. c) All calibration data including the ^{83m}Kr calibration. d) Xenon X-ray.

towards liquid-gas interface where it is extracted. The S2 signals are corrected for depth as impurities exponentially attenuate electrons drifting through the xenon (section Kr cal). The value of g2 can also be thought of as the single electron size in PE, fortunately the LUX detector is low enough in threshold to observe singe electrons being extracted from the liquid. Comparing the value of g2 derived from the Doke method with the single electron size is a good sanity check on the energy scale calibration. As the electrons are extracted from the liquid they are accelerated by larger field between the gate and anode where they electo-lumanesance, a single extracted electron creates tens to hundreds of photons which are collected by both PMT arrays. We can cut on the single electron population (small S2 pulses without an associated S1) and measure the single electron size along with the extraction efficiency efficiency. The extraction efficiency is defined as the probability that an election will be extracted from the liquid into the gas in a region of 3.5 kV between the anode and the gate. For a given event the extraction of electrons is a binomial processes with a rate approaching unity for fields above 5 kV (reference). Figure 4.9, shows the single electron size as measured by the bottom PMT array (used for S2 pulses in the LUX detector to avoid saturation). The population is modeled by a skew Gaussian due to the Poisson nature of measuring only a handful of photo electrons (PE) per extracted electron. The mean of the distribution is found to be 9.7 PE/e^- with a width of σSE= 3.6 Phe/e^-. Thus, the extraction efficiency is g2 over the single electron size and is found to be (59.3$\pm$14)%, given the extraction field the value is in good agreement with previous measurements in other xenon detectors -[2 refs extraction].

4.2 Modeling Intrinsic Detector Resolution

Intrinsic statistical fluctuations in light and charge (S1, S2) collection in the LUX detector lead to a spread in collected quanta. To measure effects from recombination

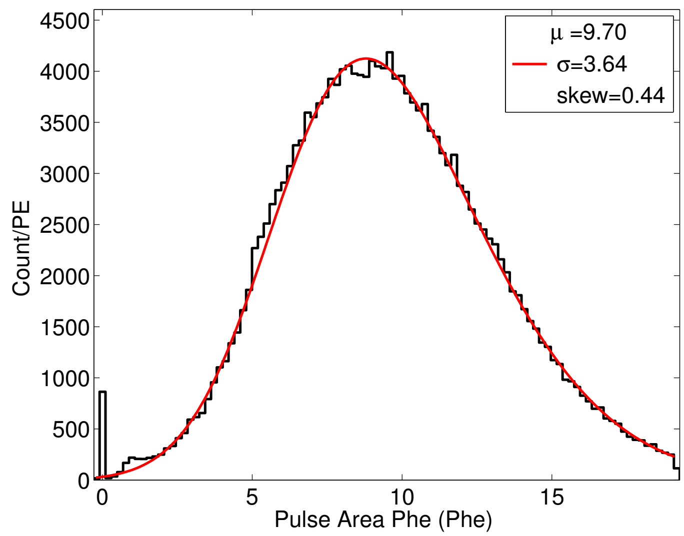

Figure 4.9: Single electron distribution as seen by the bottom PMT array fitted with a skew Gaussian model to account for the underling Poisson statistics of observing between 9 and 10 photo electrons (PE) for each electron leaving the liquid and entering to the gas phase at a higher field causing electro-luminescence. The μ of the fit represents the true mean of the skew Gaussian distribution.

fluctuations and the Fano factor we must first decouple the detector component of resolution. We use the model described in [Dahl's thesis] in which the measured scintillation and ionization signals S1, S2 (measured in Phe) are related to the number of photons and electrons by gains g1 and g2, 4.6. Specifically, the average number of photons and electrons produced for a given energy deposit are proportional to the average S1,S2 signals at a given drift field. The gain g1 represents photon detection efficiency, the probability of a photon from an energy deposit striking a PMT convolved with the quantum efficiency of the PMTs. Gain g2 represents the average S2 signal of a single electron normalized by the average single electron size. Where S2 uses only the bottom PMT array and is corrected for lifetime.

$$\begin{aligned}
\langle \mathrm{n}_\gamma \rangle &= \frac{\langle \mathrm{S1} \rangle}{\mathrm{g}_1} \\
\langle \mathrm{n}_\mathrm{e} \rangle &= \frac{\langle \mathrm{S2} \rangle}{\mathrm{g}_2}
\end{aligned} \tag{4.6}$$

The statistical fluctuations for the measured number of quanta in equation 4.6 are from the statistical processes that comprise the measured S1 and S2 signal.

$$\begin{aligned}
\sigma^2_{\mathrm{n}_{\gamma\mathrm{stat}}} &= \frac{\sigma^2_{\mathrm{S1}_\mathrm{stat}}}{\mathrm{g}_1^2} \\
\sigma^2_{\mathrm{n}_{\mathrm{e}\mathrm{stat}}} &= \frac{\sigma^2_{\mathrm{S2}_\mathrm{stat}}}{\mathrm{g}_2^2}
\end{aligned} \tag{4.7}$$

The variance in the number of photons in equation 4.7 can be broken into two parts. First, a binomial variance due to counting a fraction, g1, of the initial photons produced. $\mathrm{Var}_{\mathrm{n}_\gamma} = \frac{(1-\mathrm{g1})\times\mathrm{g1}\times\mathrm{n}_\gamma}{\mathrm{g}_1^2}$. Second, the variance in the response of the PMTs to a single photon. $\mathrm{Var}_{\mathrm{n}_\gamma} = \frac{\mathrm{g}_1\times\mathrm{n}_\gamma\times\sigma^2_{\mathrm{PE}}}{\mathrm{g}_1^2}$. Combining the two leads to the the result in equation 4.8.

$$\sigma^2_{\mathrm{n}_{\gamma\mathrm{stat}}} = \frac{1-\mathrm{g}_1+\sigma^2_{\mathrm{PE}}}{\mathrm{g}_1}\mathrm{n}_\gamma \tag{4.8}$$

The variance in the number of electrons in equation 4.7 is comprised of the following statistical uncertainties. First, a binomial variance due to the extraction efficiency of electrons from the liquid-gas interface. $\mathrm{Var}_{\mathrm{n}_\mathrm{e}} = \frac{(1-\mathrm{ext})\times\mathrm{Ext}\times\mathrm{n}_\mathrm{e}\times(\mathrm{single}_\mathrm{E})}{\mathrm{g}_2^2}$, Ext is the electron extraction probability and $\mathrm{single}_\mathrm{E}$ is the single electron size in PE. Second, the variance in the response of the PMTs to a single electron. $\mathrm{Var}_{\mathrm{n}_\mathrm{e}} = \frac{\mathrm{Ext}\times\mathrm{n}_\mathrm{e}\times\sigma^2_{\mathrm{SE}}}{\mathrm{g}_2^2}$. Finally, the additional variance from electron attenuation is modeled as a Poisson probability of electron capture in each Z slice of the detector. The variance from each Z slice depends of the average number of electrons that will be attenuated. The probability of attenuation at each slice in drift time T is $\mathrm{P(T)} = 1 - \mathrm{e}^{-\mathrm{T}/\tau}$, where τ for the data sets to be considered is 1000 μs. The drift region considered in the fiducial volume is from 38 to 304.5 μs. The average variance from events in the fiducial can be given by equation 4.9.

$$\sigma^2_{\mathrm{n_{e_{att}}}} = \mathrm{n_e} \frac{\int_{\mathrm{T_{min}}}^{\mathrm{T_{max}}} (1 - \mathrm{e}^{-\mathrm{T}/\tau}) \mathrm{dT}}{\int_{\mathrm{T_{min}}}^{\mathrm{T_{max}}} \mathrm{dT}} = 0.155 \times \mathrm{n_e} \tag{4.9}$$

Combining the variances leads to the the result for the statistical variance in the observed number of electrons equation 4.10.

$$\sigma^2_{\mathrm{n_{e_{stat}}}} = \frac{\mathrm{Ext} \times \sigma^2_{\mathrm{SE}} + (1 - \mathrm{Ext}) \times \mathrm{g2}}{\mathrm{g}_2^2} \mathrm{n_e} + \sigma^2_{\mathrm{n_{e_{att}}}} \tag{4.10}$$

For this analysis we use the following detector gains: 4.11.

$$
\begin{gathered}
\mathrm{g_1} = 0.097 \pm 0.008\,[\mathrm{Phe/n_\gamma}] \\
\mathrm{g_2} = \mathrm{SE_b} \times \mathrm{Ext} = 5.75 \pm 1.4\,[\mathrm{Phe/n_e}] \\
\mathrm{SE_b} = 9.70 \pm 0.05\,[\mathrm{Phe/n_e}] \\
\sigma\mathrm{SE_b} = 3.64\,[\mathrm{Phe/n_e}] \\
\mathrm{Ext} = 0.593 \pm 0.144 \\
\sigma_{\mathrm{PE}} = 0.51\,[\mathrm{Phe/n_\gamma}]
\end{gathered}
\tag{4.11}
$$

Combining equations 4.8-4.11 we find the intrinsic detector resolution for the average S1 and S2 signals in the LUX detector, equation 4.12. Note, the intrinsic resolution in S2 is subdominant to that of S1, since on average one electron multiplies to about ten photons detected by the bottom PMT array [ref]. Also listed in 4.13, are the instrumental fluctuations with a linear dependance on quanta measured with a global fit to mono energetic sources [next section]. The total variance in the light and charge channels is the linear combination of the statistical and instrumental variance.

$$
\begin{gathered}
\sigma_{\mathrm{n}_{\gamma_{\mathrm{stat}}}} = 3.46\sqrt{\mathrm{n}_\gamma} \\
\sigma_{\mathrm{n}_{\mathrm{e}_{\mathrm{stat}}}} = 0.68\sqrt{\mathrm{n_e}}
\end{gathered}
\tag{4.12}
$$

$$
\begin{aligned}
\sigma_{n_{\gamma_{\mathrm{inst}}}} &= \frac{6.4 \pm 1.7}{100} \times n_\gamma \\
\sigma_{n_{e_{\mathrm{inst}}}} &= \frac{6.6 \pm 0.9}{100} \times n_e
\end{aligned} \tag{4.13}
$$

$$
\begin{aligned}
\sigma^2_{n_{\gamma_{\mathrm{Det}}}} &= \sigma^2_{n_{\gamma_{\mathrm{stat}}}} + \sigma^2_{n_{\gamma_{\mathrm{inst}}}} \\
\sigma^2_{n_{e_{\mathrm{Det}}}} &= \sigma^2_{n_{e_{\mathrm{stat}}}} + \sigma^2_{n_{e_{\mathrm{inst}}}}
\end{aligned} \tag{4.14}
$$

4.3 Measuring Recombination Fluctuations

4.3.1 Measuring Recombination Fluctuations with Mono-Energetic Sources

To model recombination we start with a basic assumption that for a given energy deposit in liquid xenon the number of quanta produced is equal to the number of exitons and the number of ions. The number of ions cerated contains a spread given by a Fano factor F. The value of F for liquid xenon is small, has a theoretical value of 0.05 [**?**].

$$
\begin{aligned}
\frac{E}{W} &= n_q = n_i + n_{ex} \\
\frac{E}{W} &= n_\gamma + n_e
\end{aligned} \tag{4.15}
$$

Where E is energy in [keV], W is the work function in [keV/quanta], n_q is the number of quanta, n_i is the number of ions and n_{ex} is the number of exitons. The theoretical value of the number of exitons produced to ions is $\frac{n_{ex}}{n_i} = \alpha = 0.06$ and is not expected to change vs. energy [ref]. For the subsequent equations in this section we will simplify equations 4.15 to that in 4.16.

$$\begin{aligned} \alpha &= 0.06 \\ \mathrm{n_i} = \frac{\mathrm{E}}{\mathrm{W}}\frac{1}{(1+\alpha)} &= \frac{\mathrm{n_\gamma}+\mathrm{n_e}}{(1+\alpha)} \\ \sigma^2_{\mathrm{n_i}} &= \mathrm{F}\times\mathrm{n_i} \end{aligned} \tag{4.16}$$

Equation 4.16 gives us a simple model for the number of ions and exitons produced for a given interaction, the only spread in quanta thus far is due to a Fano factor governing the spread in initial quanta produced. We now convert ions and exitons to scintillation and ionization signals that are measured in the LUX detector, S1 and S2 respectively. Photons resulting from an energy deposit arise from the exitons that de-excite and from ions which recombine with freed electrons. The number of electrons corresponding to the energy deposit will be equal to the number of ions that did not recombine with a freed electron.

$$\begin{aligned} \mathrm{n_\gamma} = \mathrm{n_{ex}} + \mathrm{n_i}\times\mathrm{r} &= \mathrm{n_i}\times(\mathrm{r}+\alpha) \\ \mathrm{n_e} &= \mathrm{n_i}\times(1-\mathrm{r}) \\ \mathrm{r} &= \frac{\frac{\mathrm{n_\gamma}}{\mathrm{n_e}}-\alpha}{\frac{\mathrm{n_\gamma}}{\mathrm{n_e}}+1} \end{aligned} \tag{4.17}$$

Where r represents the electron-ion recombination probability. A key measurable quantity is the size of recombination probability fluctuation σ_{r}. Since we measure $\mathrm{n_\gamma}$ and $\mathrm{n_e}$ as S1 and S2 signals and not ions and exitons, an additional variance arrises from the ion-electron recombination fluctuations. These recombination fluctuations are dependent on the dE/dx of each individual electron produced making them much larger than the spread from the Fano factor. We now combine the uncertainties from the Fano factor, recombination and the statistical uncertainty from detector resolution (σ_{Det}) and solve for the observed quantities given in 4.18:

$$
\begin{aligned}
\sigma^2_{\mathrm{n}_\gamma} &= \sigma^2_{\mathrm{n_{ex}}} + \sigma^2_{\mathrm{n_i}}\mathrm{r}^2 + \sigma^2_{\mathrm{r}}\mathrm{n_i^2} + \sigma^2_{\mathrm{n}_{\gamma\mathrm{Det}}} = \sigma^2_{\mathrm{n_{ex}}} + \mathrm{n_i F(r^2)} + \sigma^2_{\mathrm{r}}\mathrm{n_i^2} + \sigma^2_{\mathrm{n}_{\gamma\mathrm{Det}}} \\
\sigma^2_{\mathrm{n_e}} &= \sigma^2_{\mathrm{n_i}}(1-\mathrm{r})^2 + \sigma^2_{\mathrm{r}}\mathrm{n_i^2} + \sigma^2_{\mathrm{n_{eDet}}} = \mathrm{n_i F}(1-\mathrm{r})^2 + \sigma^2_{\mathrm{r}}\mathrm{n_i^2} + \sigma^2_{\mathrm{n_{eDet}}}
\end{aligned}
\tag{4.18}
$$

For convenience we will work with $\mathrm{n_i} = (\mathrm{n}_\gamma + \mathrm{n_e})/(1+\alpha)$, this convention is chosen because both the Fano factor and recombination fluctuations act on number of ions and also because the number of ions are linearly related to the initial energy deposit. Using a mono energetic source and combined energy(equation 4.15) we can measure $\sigma^2_{\mathrm{n}_\gamma}$ and σ^2_{e} and σ^2_{E}. Dropping the contribution form the Fano factor and the the number of exitons it can be shown that the value recombination fluctuations $\sigma\mathrm{R}$ can be determined by rearranging equation 4.18, keeping in ming that $\sigma\mathrm{E}$ contains no recombination fluctuations. Where $\sigma\mathrm{R}$ is in units of quanta, $\sigma_{\mathrm{R}} = \mathrm{n_i}\sigma_{\mathrm{r}}$.

$$
\sigma^2_{\mathrm{R}} = \frac{1}{2}\left(\sigma^2_{\mathrm{n}_\gamma} + \sigma^2_{\mathrm{n_e}} - \frac{\sigma^2_{\mathrm{E}}}{\mathrm{W}^2}\right) \tag{4.19}
$$

Where the spread in observed quanta $\sigma^2_{\mathrm{n}_\gamma}$ and $\sigma^2_{n_e}$ result from a linear combination of the variance from detector resolution and recombination fluctuations.

$$
\begin{aligned}
\sigma^2_{\mathrm{n}_\gamma} &= \sigma^2_{\mathrm{n}_{\gamma\mathrm{Det}}} + \sigma\mathrm{R}^2 \\
\sigma^2_{\mathrm{n_e}} &= \sigma^2_{\mathrm{n_{eDet}}} + \sigma\mathrm{R}^2
\end{aligned}
\tag{4.20}
$$

We do not directly observe the fluctuation in number of photons and electrons, instead we measure the fluctuations in the corresponding S1 and S2. The fluctuation in the S1 and S2 signal when divided by the gains g1 g2 represent on average the fluctuation in photons or electrons due to detector resolutions (statistical and instrumental variance) combined with recombination fluctuations. 4.20.

$$\begin{aligned} \sigma^2_{\mathrm{n}_{\gamma_{\mathrm{Det}}}} &= \frac{\sigma^2_{\mathrm{S1}}}{\mathrm{g}_1^2} - \sigma \mathrm{R}^2 \\ \sigma^2_{\mathrm{n}_{\mathrm{e}_{\mathrm{Det}}}} &= \frac{\sigma^2_{\mathrm{S2}}}{\mathrm{g}_2^2} - \sigma \mathrm{R}^2 \end{aligned} \tag{4.21}$$

Combining equations 4.19 and 4.21 leads to the results in equation 4.22, which is a formula to directly measure recombination fluctuations using a mono energetic source.

$$\sigma^2_{\mathrm{R}} = \frac{1}{2}\left(\frac{\sigma^2_{\mathrm{S1}}}{\mathrm{g}_1^2} + \frac{\sigma^2_{\mathrm{S2}}}{\mathrm{g}_2^2} - \frac{\sigma^2_{\mathrm{E}}}{\mathrm{W}^2}\right) \tag{4.22}$$

Equations 4.22 and 4.21 gives us a method to measure recombination fluctuations along with fluctuations in n_γ and n_e due to intrinsic detector resolution, (will be discussed in the next section). It is important to note that $\sigma^2_{\mathrm{n}_\gamma}$, $\sigma^2_{\mathrm{n}_\mathrm{e}}$ and σ^2_{E} are observable quantities when using a mono energetic source. The variance in combined energy does not contain variance from recombination fluctuations as those fluctuation occur along lines of constant energy. Note, we have dropped the contribution from the Fano factor and the spread is exitons as they are much smaller than recombination fluctuations or the variances from measuring light and charge intrinsic to the detector. The observed variance in the light and charge channels

(S1, S2) is the result of two compounded random processes. After the initial charge deposit the number of charge and light quanta undergo recombination fluctuations. Subsequently, as the light or charge is collected in the detector an additional variance from detector resolution occurs. The result is the sum of two random processes thus the variance are added.

4.3.2 Results with Mono Energetic Calibration Sources

Using equation 4.22 and 4.21 along with the measurements of g1 g2, we construct a combined energy and deconvolve the recombination fluctuations from variances in the light and charge channel of the detector. The result is shown in figure 4.10, the black white and red lines represent σR, $\sigma \mathrm{n}_{\gamma_{\mathrm{Det}}}$, $\sigma \mathrm{n}_{\mathrm{e}_{\mathrm{Det}}}$, respectively for sources listed in Table 4.1. A variance with a linear and root term is fit to the data and used to extract instrumental fluctuations and constrain the statistical fluctuations. The linear term corresponds to instrumental fluctuations and the root term corresponds to statistical fluctuations. Instrumental fluctuations go like the signal size and may potentially be due to ripples in the liquid surface caused by xenon bubbles or other systematics that are unaccounted for. The root term should result purely from counting photo electrons, described earlier. We find:

$$\begin{aligned} \sigma^2_{\mathrm{n}_{\gamma_{\mathrm{Det}}}} &= \sigma^2_{\mathrm{n}_{\gamma_{\mathrm{Stat}}}} + \sigma^2_{\mathrm{n}_{\gamma_{\mathrm{Inst}}}} = \left(0 \pm 10 \cdot \sqrt{\mathrm{n}_\gamma}\right)^2 + ((6.4 \pm 1.8)/100 \cdot \mathrm{n}_\gamma)^2 \\ \sigma^2_{\mathrm{n}_{\mathrm{e}_{\mathrm{Det}}}} &= \sigma^2_{\mathrm{n}_{\mathrm{e}_{\mathrm{Stat}}}} + \sigma^2_{\mathrm{n}_{\mathrm{e}_{\mathrm{Inst}}}} = (1 \pm 4 \cdot \sqrt{\mathrm{n}_\mathrm{e}})^2 + ((6.6 \pm 0.6)/100 \cdot \mathrm{n}_\mathrm{e})^2 \\ \sigma^2_{\mathrm{R}} &= ((5.5 \pm 0.5)/100 \cdot \mathrm{n}_\mathrm{q})^2 \end{aligned} \tag{4.23}$$

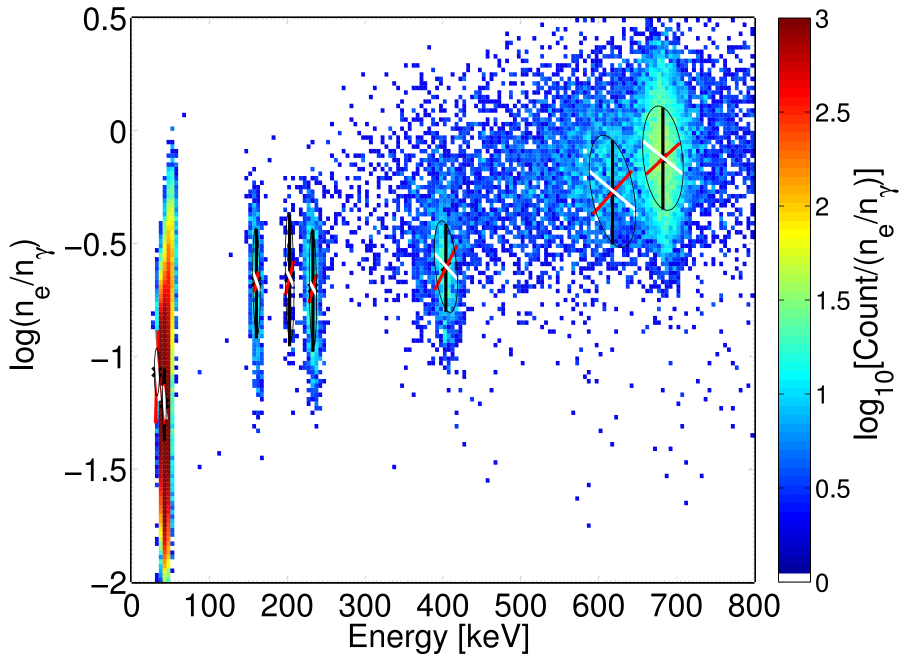

Figure 4.10: Populations of calibration sources in discrimination space $\log\left(\frac{\mathrm{n_e}}{\mathrm{n_\gamma}}\right)$ vs. combined energy [$\mathrm{keV_{ee}}$]. The ovals represent the combination of σR, $\sigma \mathrm{n}_{\gamma_{\mathrm{Det}}}$, $\sigma \mathrm{n}_{\mathrm{e}_{\mathrm{Det}}}$ in black, white, red respectively.

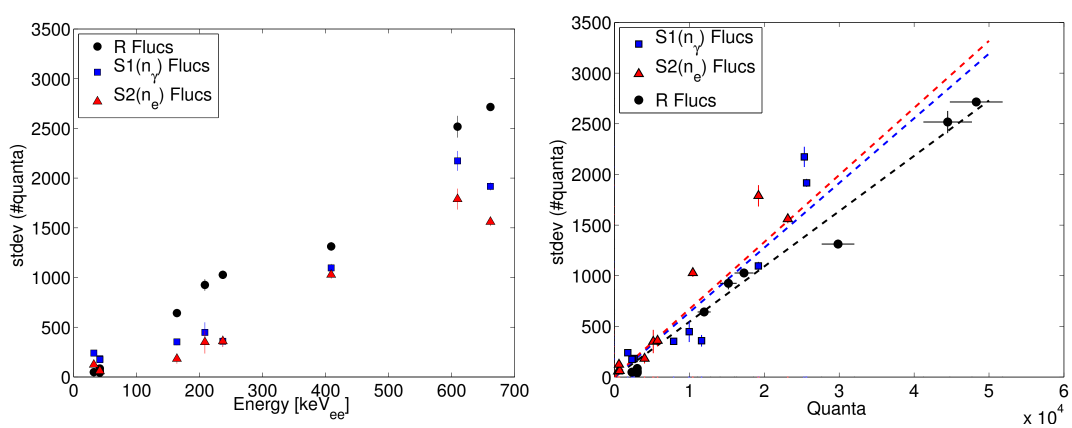

Figure 4.11: Measured values of σR, $\sigma \mathrm{n}_{\gamma_{\mathrm{Det}}}$, $\sigma \mathrm{n}_{\mathrm{e}_{\mathrm{Det}}}$ vs. Energy on the left and vs. Quanta on the right. Measured using sources listed in Table 4.1.

4.3.3 Measuring Recombination Fluctuations in Desecrate Energy Bins

The pervious subsection demonstrated the power of using a mono energetic source measure recombination fluctuations, equation 4.19. In this section we present a method to decouple statistical variance from recombination fluctuations when confined to an energy bin of width Δ_{E}. The consideration of desecrate binning is crucial when dealing with a continual energy spectrum. Take the tritium beta spectrum as an example, we lose the ability to independently measure $\sigma^2_{\mathrm{n}_\gamma}$, $\sigma^2_{\mathrm{n_e}}$, σ^2_{E} and are only left with a smear of n_γ, $\mathrm{n_e}$, E. However, there are two key pieces of information still left at our disposal. First, the combined energy can be reconstructed from global fits to g1 and g2, and even corrected for spectral shape and detector resolution (discussed later in section [link]). Second, we can calculate values of statistical variance for the light and charge channels as a function of energy, described in 4.12, 4.13. It will be shown in this section that having a priori knowledge of g1,g2 and the functional for of the statistical variance from detector resolution will be sufficient to measure recombination fluctuations for a continual energy spectrum binned in energy with width Δ_{E}.

We begin the treatment of binning with the the case of having a finite bin width around the central combined energy of a mono energetic source. First, we quantify the change in the statistical components of equation 4.18 when slicing out a bin in combined energy space. The slice in combined energy is illustrated for a toy model at quanta corresponding to that of the combined 41.6 keV ^{83}Kr decay in Figure 4.12. All contribution from recombination fluctuations are included when slicing out a section of combined energy, illustrated in Figure 4.12. However, the slice contains only a reduced statistical component from both the light and charge signals, and in the limit that ΔE goes to zero the statistical component of light and charge converge to a value defined as χ_{stat} (where χ is the measured σ in a bin of combined energy). To solve for the value of χ_{stat} we first calculate the slope induced by statistical variance in the number of photons vs. quanta and the complementary slope of electrons vs. quanta, defined as M and 1-M respectively. The value of M depends on the magnitude of the statistical variances and is given in equation 4.24. The sum of the two slopes must equal one as the sum of photons and electors make up combined energy.

$$\begin{aligned} \mathrm{M} = \tan(\theta_{\mathrm{n}_{\gamma\mathrm{Det}}}) &= \frac{\sigma^2_{\mathrm{n}_{\gamma\mathrm{Det}}}}{\sigma^2_{\mathrm{n}_{\gamma\mathrm{Det}}} + \sigma^2_{\mathrm{n}_{\gamma\mathrm{Det}}}} \\ 1 - \mathrm{M} = \tan(\theta_{\mathrm{n}_{\mathrm{eDet}}}) &= \frac{\sigma^2_{\mathrm{n}_{\mathrm{eDet}}}}{\sigma^2_{\mathrm{n}_{\gamma\mathrm{Det}}} + \sigma^2_{\mathrm{n}_{\gamma\mathrm{Det}}}} \end{aligned} \tag{4.24}$$

With the slope between combined energy and $\sigma_{\mathrm{n}_{\gamma\mathrm{Det}}}$ and between energy and $\sigma_{\mathrm{n}_{\mathrm{eDet}}}$ defined in equation 4.24 the value of the shared statistical uncertainty in combined energy space can be determined. We first treat the case of $\Delta\mathrm{E} = 0$ in equation 4.25 which is also valid when the centroid of light yield and change yield has been subtracted (discussed later).

$$\chi^2_{\mathrm{Det}} = \mathrm{M}^2\sigma^2_{\mathrm{n}_{\mathrm{eDet}}} + (1 - \mathrm{M})^2\sigma^2_{\mathrm{n}_{\gamma\mathrm{Det}}} \tag{4.25}$$

The variable χ is used to represent the observed σ when dealing in bins of

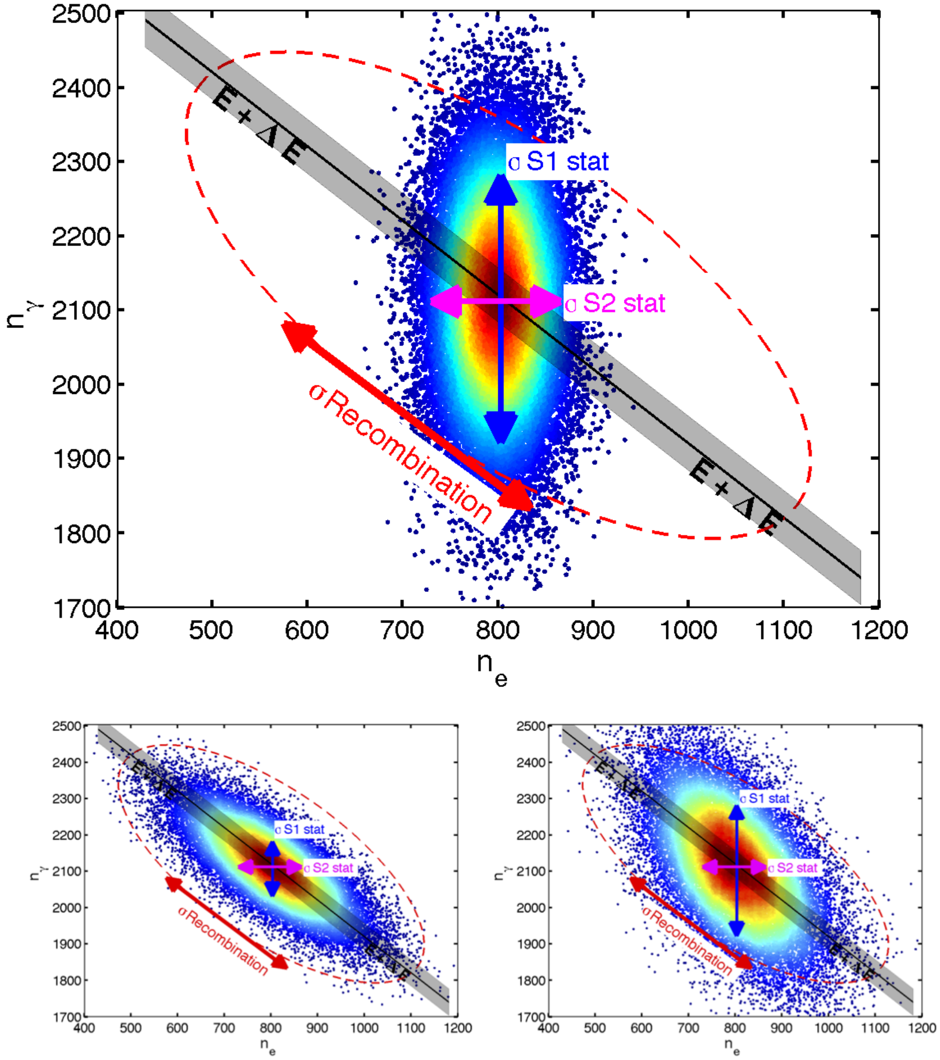

Figure 4.12: Top: Illustration of statistical variance, recombination fluctuations are set to 0. The spread in number of photons moves vertically and the spread in number of electrons moves horizontally. In black, a line of constant energy along the mean of combined energy with a width ΔE. Bottom left: Dominated by recombination fluctuations which move 45° to statistical variances. Bottom Right: Typical values for recombination and S1, S2 Stat for Kr^{83}.

combined energy. Let's briefly consider the implication of equation 4.25. For the case of $\sigma^2_{\mathrm{n_{e_{Det}}}} = \sigma^2_{\mathrm{n_{\gamma_{Det}}}}$, M=0.5, resulting in $\sigma^2_{\mathrm{n_{e_{Det}}}} = \sigma^2_{\mathrm{n_{\gamma_{Det}}}} = \chi^2_{\mathrm{Det}}$. This case can be thought of as sweeping out equal variance from the statistical population which would for a circle as illustrated in Figure 4.12. For the case of $\sigma^2_{\mathrm{n_{e_{Det}}}} \neq \sigma^2_{\mathrm{n_{\gamma_{Det}}}}$ the observed statistical variance in a slice of combined energy will become less than the variance of the best channel. Specifically for the LUX detector the implication of equation 4.25 is that the statistical variance measured in a slice of combined energy will collapse to less than that of the S2 statistical uncertainty, as bin width Δ_{E} goes to zero.

To complete the treatment of binned energy in this section we now add the final piece to the observed statistical variance, the contribution from the bin width Δ_{E}. The residual variance arrises from rotating the population of 2D gaussian about the bin center, the rotation having a slope of M or (1-M) as given in equation 4.24. Note, the residual term from the slope can also be removed by centroid subtraction of the photons and electrons vs. energy as discussed later in section 4.3.7, in that case we are only left with χ^2_{Det} shared between the two channels.

$$
\begin{aligned}
\chi^2_{\mathrm{n_{\gamma_{Det}}}} &= \chi^2_{\mathrm{Det}} + \frac{(\mathrm{MW}\Delta_{\mathrm{E}})^2}{12} \\
\chi^2_{\mathrm{n_{e_{Det}}}} &= \chi^2_{\mathrm{Det}} + \frac{((1-\mathrm{M})\mathrm{W}\Delta_{\mathrm{E}})^2}{12}
\end{aligned} \tag{4.26}
$$

Were χ^2 is defined in 4.25, M is given in equation 4.24, W is the work function in [quanta/keV], Δ_{E} is a bin of energy [keV], the normalization of 12 arrises from the second moment of a rotated line about its center. The total observed variance,

χ^2, in the number of photons and electrons considering a bin of combined energy can now be determined transforming equation 4.18 to 4.27.

$$\begin{aligned}\chi^2_{n_\gamma} &= \sigma^2_{n_{ex}} + n_i F(r)^2 + \sigma^2_r n_i^2 + \chi^2_{n_{\gamma Det}} \\ \chi^2_{n_e} &= n_i F(1-r)^2 + \sigma^2_r n_i^2 + \chi^2_{n_{e Det}}\end{aligned} \tag{4.27}$$

In equation 4.27 we have defined the observed standard deviation in units of quanta χ for n_γ, n_e when working with bins of combined energy. In the limit that F, $\sigma^2_{n_{ex}}$ and Δ_E go to zero the observed variance in number of photons and electrons (χ_{n_γ} and χ_{n_e}) are related to the size of recombination fluctuations in a given combined energy bin, equation 4.28. Where σR is in units of quanta, $\sigma_R = n_i \sigma_r$.

$$\begin{aligned}\sigma^2_{R_\gamma} &= \chi^2_{n_\gamma} - \chi^2_{n_{\gamma Det}} \\ \sigma^2_{R_e} &= \chi^2_{n_e} - \chi^2_{n_{e Det}}\end{aligned} \tag{4.28}$$

We have arrived at the conclusion of this section, armed with equation 4.28 we now have two methods for determining the size of recombination fluctuations, σ^2_R where the subscript γ or e is used to represent the channel of quanta used for the calculation. Either the observed variance in the light and charge channel can be used to measure the size of recombination fluctuation in a bin of energy. Any asymmetry between the two methods has implications which are discussed in the following subsection.

4.3.4 Measuring the Fano Factor in Bins of Energy

There are three terms in equation 4.27 that give rise to an asymmetry between the observed variance $\sigma^2_{\mathrm{R}_\gamma}$ and $\sigma^2_{\mathrm{R_e}}$. The small difference in variance from the slope can be solved for exactly leaving just the Fano factor F and $\sigma^2_{\mathrm{n_{ex}}}$. By taking the difference of variance in the two channels component of recombination variance drops out leaving only the Fano factor and the variance in number of exitons, given in equation 4.27.

$$\sigma^2_{\mathrm{R}_\gamma} - \sigma^2_{\mathrm{R_e}} = \sigma^2_{\mathrm{n_{ex}}} + \mathrm{n_i F(2r - 1)} \tag{4.29}$$

F is the Fano factor, equation 4.16, $\sigma^2_{\mathrm{n_{ex}}}$ is the variance of the number of exitons produced and r is the recombination fraction, equation 4.17. Consider the case such that variance in the number of exitons $\sigma^2_{\mathrm{n_{ex}}}$ is much less than the contribution from the Fano factor. In such a regime we can solve for the Fano factor, potentially energy dependent, from equations 4.29.

$$\mathrm{F(E)} = \frac{\sigma^2_{\mathrm{R}_\gamma} - \sigma^2_{\mathrm{R_e}}}{\mathrm{n_i(2r-1)}} \begin{cases} \mathrm{r} \neq \frac{1}{2} \end{cases} \tag{4.30}$$

There is an underlying subtlety to equation 4.30. Remarkably, in the limit that Δ_{E} goes to zero the Fano factor can be extracted with minimal knowledge of intrinsic detector statistical variance. Further, when the statistical variance of S1 and S2 are identical the value of M (equation **??**) will be 0.5. In that special case no knowledge of the statistical variance is needed to measure the Fano factor.

When $\mathrm{r} = \frac{1}{2}$ the coefficient in front of the Fano factor becomes zero in equation

4.29. At this value an equal contribution from the Fano factor goes into the variance χ^2 of photons and electrons, allowing for the smaller value of σ^2_{ex} to be extracted.

$$\sigma^2_{\mathrm{n_{ex}}} = \sigma^2_{\mathrm{R}_\gamma} - \sigma^2_{\mathrm{R_e}} \begin{cases} \mathrm{r} = \frac{1}{2} || \sigma^2_{\mathrm{n_{ex}}} >> \mathrm{n_i F(2r-1)} \end{cases} \tag{4.31}$$

Equation 4.31 is also valid in the case that $\sigma^2_{\mathrm{n_{ex}}}$ is much larger than the contribution form the Fano factor. This happens to be true when dealing with the time dependent light yield of $^{83\mathrm{m}}$Kr, this topic will be explored in the next section.

4.3.5 Application to ^{83}Kr

Using the high stats Kr83 calibration data we can validate the method for working in a bin of energy since the exact solution for recombination and detector fluctuations can be measured, as outlined in section 4.3.1 and 4.3.3. Once the fluctuations from detector resolution are measured in the light and charge channel (S1 and S2 signals), the asymmetry between the two channels can be used to calculate the Fano factor (equation 4.27). The asymmetry in fluctuations in the light and charge channel arrises from the Fano factor acting on ion production which is later amplified through the recombination fraction, as long as the recombination fraction does not equal 0.5. For the case of the $^{83\mathrm{m}}$Kr calibration the recombination fraction was 0.772 resulting in recombination fluctuations of 3 to 4 more quanta in the light channel as compared to the charge channel, see table 4.4. Though the additional recombination fluctuation is small having ample statistics the Fano factor can be constrained. The errors in the measurement were derived from simulated Kr data sets of 400,000 events with the Fano factor turned off, using 100 trials. First, recombination fluctuations were turned off and only fluctuations from detector resolution as calculated in section 4.3.1 were used, see Table 4.2. It was found that the error of the difference in recombination fluctuation from the light and charge channel (sigma$^2_{\mathrm{R}_\gamma}$ and $\sigma^2_{R_e}$) along with the error in ion production and recombination fraction were enough to constrain the Fano factor to 0.001-0.003. Next, the value of recombination was set slightly higher than the actual value of 82 to 100 quanta and the trials were repeated, see table 4.3. With the addition of recombination fluctuations to detector resolution fluctuations the error on measuring the Fano factor grew to 0.002-0.009, with smaller bin sizes (ΔE around the center leading to the smallest error as seen from equation 4.26.

The results of the high stats calibration data are shown in table 4.4, containing 400k events in the fiducial volume of the detector. Using equation 4.28 we find good agreement between the method described in equation 4.19 and the recombination fluctuation calculated from the charge channel ($\sigma_{\mathrm{R}_\gamma}$ and $\sigma_{\mathrm{R_e}}$). The accuracy helps us build confidence that the statistical components of the detector are modeled well enough to measure recombination fluctuation to within 3%. Further, the ability to see the asymmetry in recombination fluctuations between the light and charge channel demonstrates the power of using binned combined energy (section 4.3.3). Any observed difference between the two channels can only be from either the Fano factor or spread in exiton production, but we assume the fluctuations in exiton production are much less than fluctuations in ion production. The Fano factor is derived from equations 4.30 and the uncertainty was determined from simulations.

Δ_{E} [keV]	Count	$\sigma(\sigma^2_{\mathrm{R}_\gamma})$	$\sigma(\sigma^2_{\mathrm{R_e}})$	$\sigma(\sigma^2_{\mathrm{R}_\gamma} - \sigma^2_{\mathrm{R_e}})$	σF
0.025	1528	77.8	77.9	1.3	0.0008
0.05	3063	54.4	54.6	1.8	0.0012
0.1	6128	36.4	36.6	2.6	0.0016
0.2	12242	23.7	23.8	3.7	0.0023
0.25	15290	22.9	22.9	4.0	0.0026
0.5	30528	17.5	17.5	5.2	0.0033

Table 4.2: Values for the standard deviation of the observed value of σ^2_{R} from n_γ and $\mathrm{n_e}$ along with the standard deviation of the difference, for a simulated $^{83\mathrm{m}}$Kr decay with recombination set to zero. Note, since the two methods for determining σ^2_{R} are correlated the standard deviation of the measured difference is small leading to an improved error when calculating the Fano factor or $\sigma^2_{\mathrm{n_{ex}}}$.

The total fluctuation as number of quanta is listed in the rightmost column. The Fano factor manifests itself as an asymmetry between fluctuations in the light and charge channel as given in equation 4.27, the recombination fraction was found to be r= 0.772 and the average number of ions produced per decay was $\mathrm{n_i} = 2900$. Having demonstrated the method for a mono energetic calibration source the next step will be to apply the method on the continuous beta spectrum of the tritium data.

Δ_{E} [keV]	Count	$\sigma(\sigma^2_{\mathrm{R}_\gamma})$	$\sigma(\sigma^2_{\mathrm{R_e}})$	$\sigma(\sigma^2_{\mathrm{R}_\gamma} - \sigma^2_{\mathrm{R_e}})$	σF
0.025	1523	498	498	3.2	0.0020
0.05	3056	347	347	4.1	0.0026
0.1	6118	237	237	5.3	0.0033
0.2	12225	171	171	8.6	0.0054
0.25	15285	149	148	9.5	0.0060
0.5	30514	101	99.4	14.3	0.0090

Table 4.3: Values for the standard deviation of the observed value of σ^2_{R} from n_γ and $\mathrm{n_e}$ along with the standard deviation of the difference, for a simulated $^{83\mathrm{m}}$Kr decay with recombination set to 100 quanta. Note, since the two methods for determining σ^2_{R} are correlated the standard deviation of the measured difference is small leading to an improved error when calculating the Fano factor or $\sigma^2_{\mathrm{n_{ex}}}$.

4.3.6 Application to Tritium Data (any continus spectrum)

Adapting the equation of the previous section to continuous energy spectra requires that the centriod of a continue spectrum be subtracted off so that the variance from the light yield or charge yield vs. energy is removed. ...

After applying the Smearing Model of Section 4 we apply the method described in this section to extract recombination fluctuations form the tritium data.

In this subsection we test method outlined in section 4.3.3 for dealing in bins of combined energy specifically applied to the tritium beta spectrum, but the method

σ_{R} 4.19 (Quanta)	Δ_{E} (keV)	Count	$\sigma_{\mathrm{R}_\gamma} = \sqrt{\chi^2_{\mathrm{n}_\gamma} - \chi^2_{\mathrm{n}_{\gamma\mathrm{Det}}}}$ (Quanta)	$\sigma_{\mathrm{R_e}} = \sqrt{\chi^2_{\mathrm{n_e}} - \chi^2_{\mathrm{n_{eDet}}}}$ (Quanta)	$\mathrm{F} = \frac{\sigma^2_{\mathrm{R}_\gamma} - \sigma^2_{\mathrm{R_e}}}{\mathrm{n_i}(2\mathrm{r}-1)}$ (Quanta)	$\sqrt{\mathrm{Fn_i}}$ (Quanta)
82.4 ± 4.0	0.025	1518	87.2 ± 2.9	87.1 ± 2.9	0.010 ± 0.002	5.8 ± 0.5
	0.05	3124	85.0 ± 2.0	84.9 ± 2.0	0.005 ± 0.003	3.8 ± 1.1
	0.1	6269	87.8 ± 1.3	87.6 ± 1.3	0.023 ± 0.003	8.1 ± 0.5
	0.2	12508	90.0 ± 1.0	89.7 ± 1.0	0.021 ± 0.005	7.8 ± 0.9
	0.25	15557	88.5 ± 0.8	88.3 ± 0.8	0.013 ± 0.006	6.1 ± 1.3
	0.5	30826	87.0 ± 0.6	86.7 ± 0.6	0.027 ± 0.009	8.8 ± 2.2

Table 4.4: Values for the standard deviation of the observed value of σ^2_{R} from n_γ and $\mathrm{n_e}$ along with the standard deviation of the difference, for a $^{83\mathrm{m}}$Kr data set with 400k events in the fiducial volume. The Fano factor is derived from equations 4.30 and the uncertainty was determined from simulations. The total fluctuation as number of quanta is listed in the rightmost column. The Fano factor manifests itself as an asymmetry between fluctuations in the light and charge channel as given in equation 4.27, with a recombination fraction of 0.772 and $\mathrm{n_i} = 2900$.

outlined can be used for any continue spectrum. To first order the treatment of the continuous spectrum is identical to that outlined for the mono energetic source as outlined previously in subsection 4.3.3. Figure 4.13 illustrates a tritium beta spectrum convolved with detector resolution similar to that measured for the LUX detector, the figure is analogous to Figure 4.12. As the bin size around a value of combined energy is squeezed to zero the statistical variance in the number of photons and electrons converge, the value is given by equation 4.26. Whereas, regardless of bin size recombination fluctuations remain since they move along lines of constant energy. In order to adapt the methodology developed for a mono energetic source to a continuous energy spectra requires that the centriod of the light and charge yield be subtracted off. The slope in the light and charge channels from the fundamental yield induce a further variance on top of χ_{Det} from the population in an energy bin being tilted as demonstrated in figure 4.14. For the purposes of this study, we find it sufficient to fit a quadratic form to the centroid of the entire population and subtract off the local slope from the measured variance. An analogous methods for centriod subtraction to extract recombination fluctuations are described in detail in [Patrick's Thesis].

4.3.7 Centriod Subtraction

For the case of a continuous source we expand upon the result from section 4.3.3 where the additional variance from detector resolution was calculated per energy bin as $\chi^2_{\mathrm{n}_{\gamma_{\mathrm{Det}}}}$ and $\chi^2_{\mathrm{n}_{\mathrm{e}_{\mathrm{Det}}}}$. When dealing with a continuous source we must subtract off the centroid of the number of photons and electron vs. energy to remove additional variance induced by the slope. What results is a common variance from detector resolution shared by both the charge and light channel in each bin of energy, defined as $\chi^2_{\mathrm{Det}} = \chi^2_{\mathrm{n}_{\gamma_{\mathrm{Det}}}} = \chi^2_{\mathrm{n}_{\mathrm{e}_{\mathrm{Det}}}}$, equation 4.32. The value of χ^2_{Det} is derived in 4.33 for a small variation in $\mathrm{n_e}$ around combined energy, and is identical to that found for the case of the mono energetic source in equation 4.25. This is analogous to saying that the centroid subtraction is removing the additional variance from the slope of

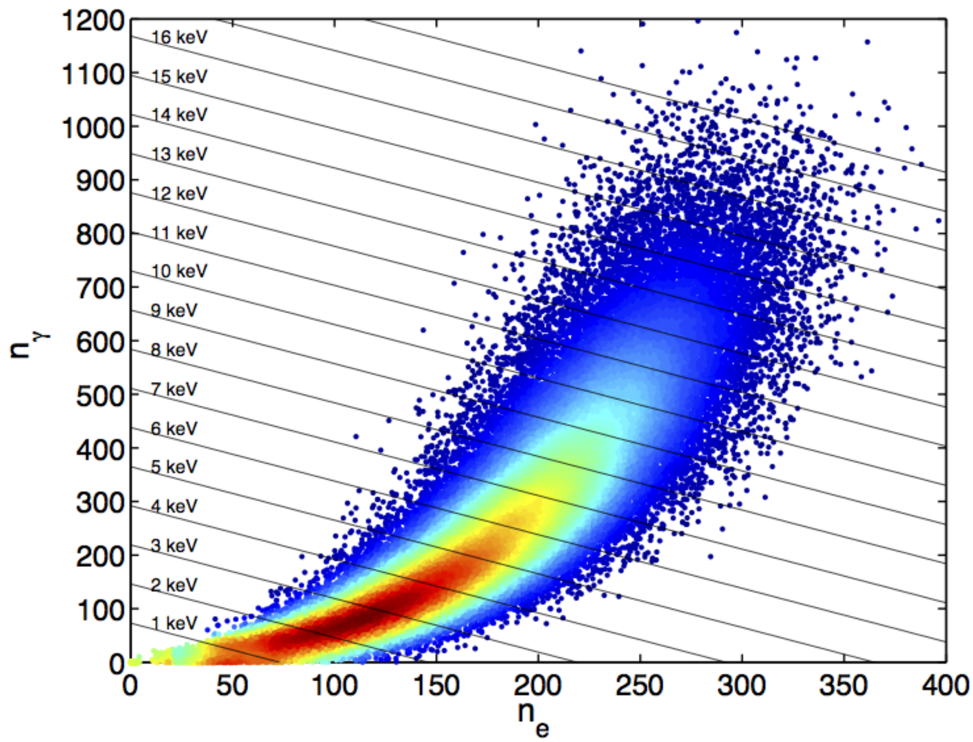

Figure 4.13: Illustration of statistical variance for the tritium beta spectrum, recombination fluctuations are set to 0. This plot is analogous to Figure 4.12 which illustrates the case for the mono energetic ^{83m}Kr decay. Recombination fluctuation move along lines of constant energy, S1 statistical fluctuation move vertically and S2 statistical fluctuations move horizontally.

light field and charge yield. The local slope of n_e with respect to quanta ($n_\gamma + n_e$) is (1-M), given in 4.24. To demonstrate the effectiveness of the method we use the measured detector resolution along with a test recombination fluctuation and simulate a tritium spectrum. The result of extracting recombination is shown in figure 4.15 for various energy bin widths. As long as the recombination is greater than χ_{Det}, which is being added in quadrature, the value of recombination can be determined to good precision using the method. The small deviation around the

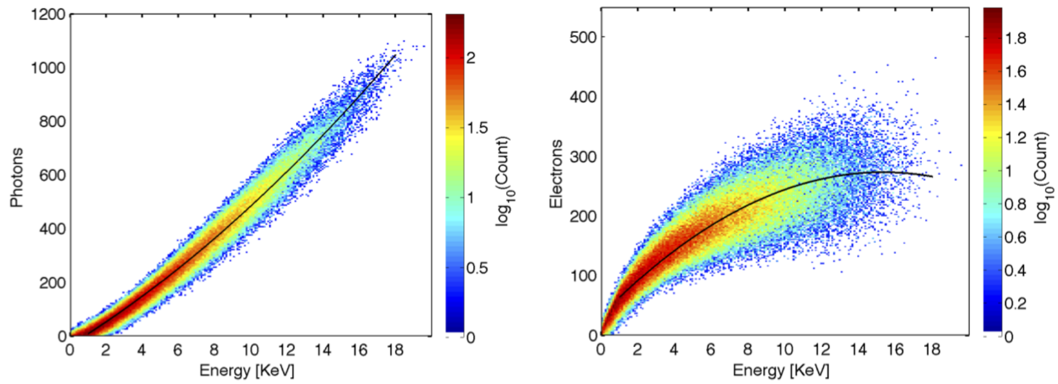

Figure 4.14: Light yield (left) and Charge yield (right) of a simulated tritium spectrum, with the fit to the centroid show in black. The variance in number of photon and electrons per energy bin is used to extract recombination fluctuations.

first and last bins is due to the spectral shape, a correction for spectral shape will be discussed in the next section and will improve the measurement of σ_{R}. The analytic solution for extracting recombination given in equation 4.32 is sufficient to first order, we ignore second order corrections in this analysis. After correcting observables for the tritium beta spectral shape we will be ready to use the tools of this section to decouple detector resolution and measure recombination fluctuations from the tritium data

$$\begin{aligned}\sigma^2_{\mathrm{R}_\gamma} &= \chi^2_{\mathrm{n}_\gamma} - \chi^2_{\mathrm{Det}} \\ \sigma^2_{\mathrm{R_e}} &= \chi^2_{\mathrm{n_e}} - \chi^2_{\mathrm{Det}}\end{aligned} \tag{4.32}$$

$$
\begin{aligned}
\delta[\Delta n_e] &= \delta[n_e] - \delta\left[\langle n_e\rangle_{n_e+n_\gamma}\right] \\
&= \overbrace{\cancel{\frac{dn_e}{dn_e}}}^{1}\delta[n_e] + \overbrace{\cancel{\frac{dn_e}{dn_\gamma}}}^{0}\delta[n_\gamma] - \delta\left[\langle n_e\rangle_{n_e+n_\gamma}\right] \\
&= \delta[n_e] - \frac{d\langle n_e\rangle}{d(n_e+n_\gamma)}\frac{d(n_e+n_\gamma)}{dn_e}\delta[n_e] - \frac{d\langle n_e\rangle}{d(n_e+n_\gamma)}\frac{d(n_e+n_\gamma)}{dn_\gamma}\delta[n_\gamma] \\
\delta[\Delta n_e] &= \delta[n_e] - (\delta[n_\gamma] + \delta[n_e])\,\frac{d\langle n_e+n_\gamma\rangle}{d\,(n_e+n_\gamma)} \\
\delta[\Delta n_e] &= (M)\delta[n_e] - (1-M)\delta[n_\gamma] \\
\chi^2_{Det} = Var(\Delta n_e) &= (M)^2\delta^2[n_e] + (1-M)^2\delta^2[n_\gamma] - 2M(1-M)\overbrace{\cancel{\delta[n_e]\delta[n_\gamma]}}^{0}
\end{aligned}
\tag{4.33}
$$

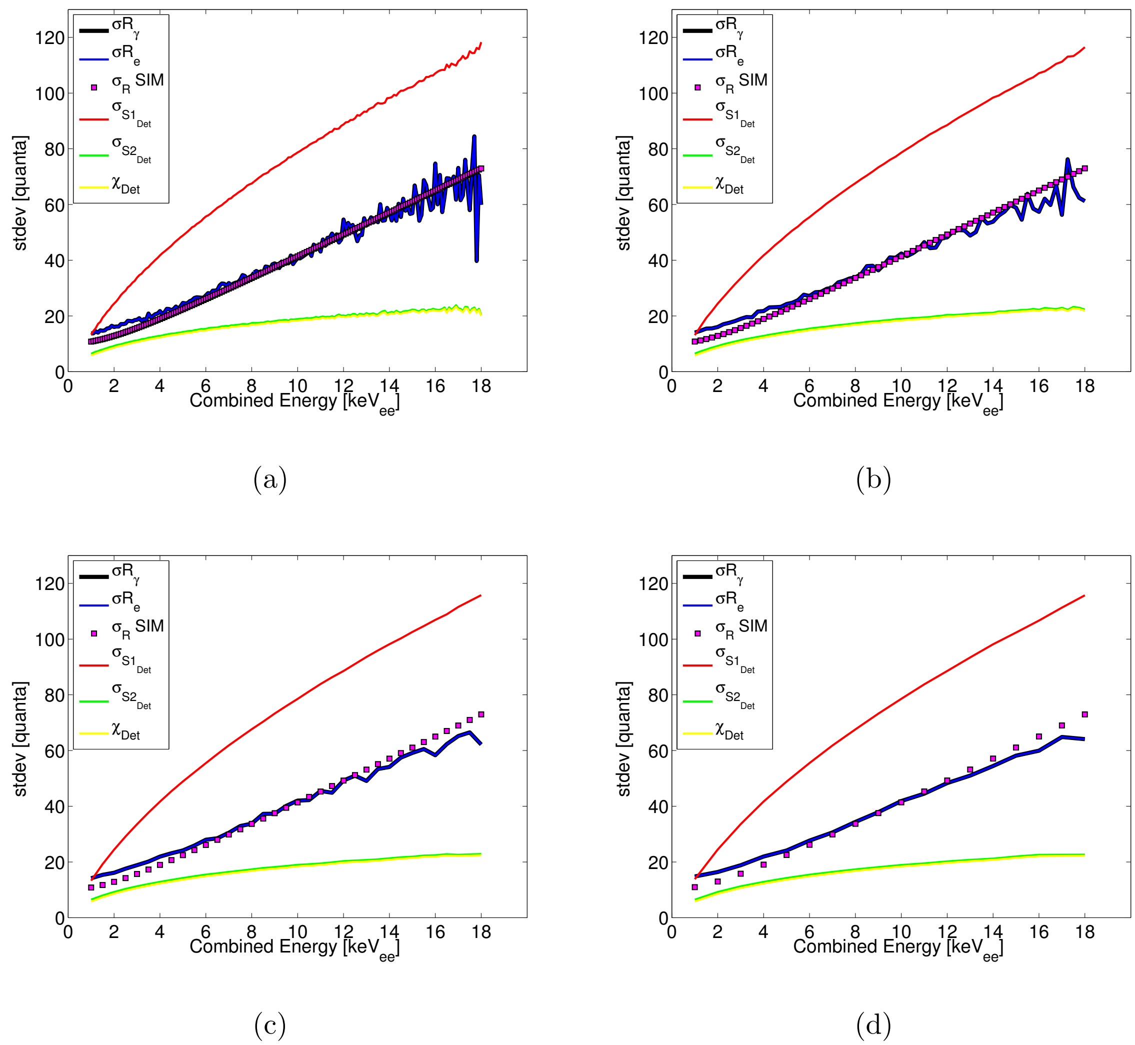

Figure 4.15: Simulated tritium spectrum with the detector resolution of the LUX detector, $\sigma_{\mathrm{S1_{Det}}}$ and $\sigma_{\mathrm{S2_{Det}}}$, and an arbitrary recombination fluctuation σR (magenta). After centroid subtraction we apply the methodology described in the previous section to extract σR (black and blue) through the light and charge channel using our knowledge of detector resolution per each energy bin χ_{Det} (green), $\mathrm{S1_{Det}}$ (red) and $\mathrm{S2_{Det}}$(yellow). The plots show cases for various bin widths in [KeV]: a) ΔE = 0.1 b) ΔE = 0.25 c) ΔE = 0.5 d) ΔE = 1.

4.4 Correcting the Tritium Spectral Shape for Finite Resolution

The goal of the following two sections is to extract light yield, charge yield and recombination fluctuations from the tritium spectrum using the methods described in section 4.3.3. The first step is to use the NEST model in an attempt to undue the effect of the tritium spectral shape and finite detector resolution, described in this section. We find that the light yield and charge yields extracted from the data deviate too much to apply the correction factor. Since the correction is found to be small we can proceed to extract new LY, QY and σR from the tritium data without correction building a model that better reproduces the data than the NEST model (which has yet to be vetted at our electric field and energy). We then take that improved model and apply the correction.

The distribution of tritium events convolved with the detector's finite resolution for S1 (scintillation) and S2 (ionization) causes the observed mean to shift from the actual mean. The shift is non trivial and depends on the spectral shape and the functional form resolution over a range of energies. A large negative derivative of the spectral shape will tend to pull the observed spectrum to lower values, and the functional form of the of resolution will also shift the spectrum. Figure 4.16 and equations 4.35,4.38 demonstrate a simple model to solve for the relation between observed mean and actual mean. Take for example a linearly declining distribution, starting with infinite detector resolution we set up bins of width Δx. To account for finite energy resolution we distribute the counts in each rectangular bin into Gaussians centered at μ_{i}, with a spread of σ_i, and normalized to the area of the bin

$N_i \times \Delta x$ with amplitude c_i. Each rectangular bin(i) can be written as a Gaussian G(i):

$$
\begin{aligned}
c_i &= \frac{N_i \times \Delta x}{\sigma_i \sqrt{2\pi}} \\
G_i(x) &= c_i \times \exp\left(\frac{-(x-\mu_i)^2}{2\sigma_i^2}\right)
\end{aligned}
\tag{4.34}
$$

Where N_i is the count in the i^{th} bin, Δx is the bin width, μ_i is the bin center and σ_i is the resolution at the i^{th} bin. Figure 4.16 show the application of equation 4.34 to a linear energy distribution with a $\sqrt{E}$ dependent σ. The observed distribution is the sum of the Gaussians, shown in red.

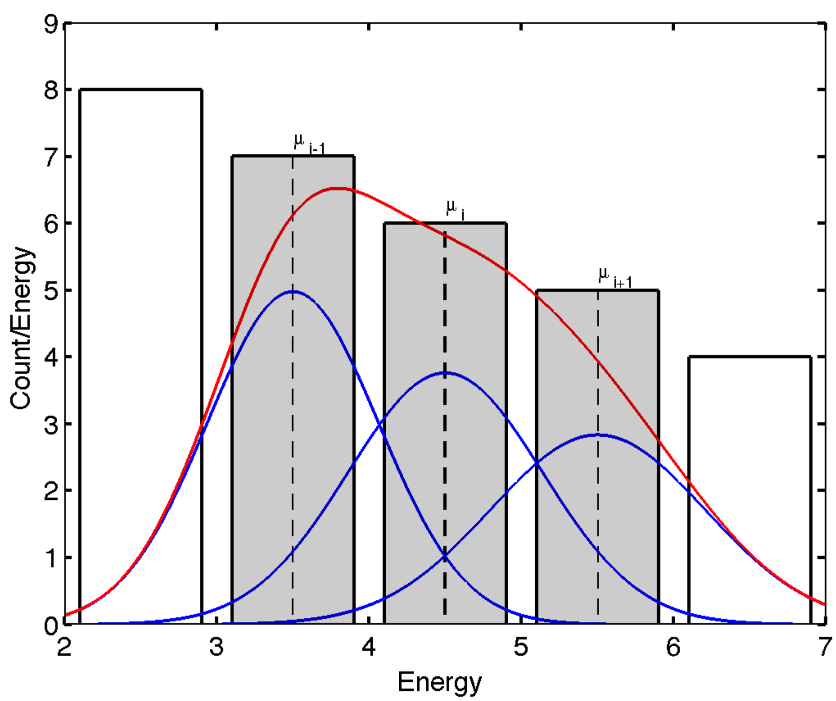

Figure 4.16

4.4.1 Calculating the Observed Energy

After modeling the finite resolution with Gaussians the mean observed at each bin can be calculated from the overlap of all bins weighted by the corresponding means. We can write the observed mean in the $\mathrm{i^{th}}$ bin, ν_i, in terms of the bin centers μ and overlapping areas of all bins using equation 4.34:

$$\nu_i = \frac{\sum_{j=1}^{n} \mu_j \int\limits_{\mu_i - \frac{\Delta x}{2}}^{\mu_i + \frac{\Delta x}{2}} G_j(x)\,\mathrm{d}x}{\sum_{j=1}^{n} \int\limits_{\mu_i - \frac{\Delta x}{2}}^{\mu_i + \frac{\Delta x}{2}} G_j(x)\,\mathrm{d}x} \tag{4.35}$$

Equation 4.35 can be solved in terms of error function and complimentary error function, first we will generalize a formula to solve for the overlapping area from the $\mathrm{j^{th}}$ bin into the $\mathrm{i^{th}}$ bin.

$$\mathrm{A_{i,j}} = \int\limits_{\mu_i - \frac{\Delta x}{2}}^{\mu_i + \frac{\Delta x}{2}} G_j(x)\,\mathrm{d}x = \begin{cases} \mathrm{c_i}\ \mathrm{erf}\left(\frac{\Delta \mathrm{x}}{\sigma_\mathrm{i}\sqrt{2}}\right), & j = i \\ \\ \frac{\mathrm{c_j}}{2}\mathrm{erfc}\left(\frac{|\mu_\mathrm{j} - \mu_\mathrm{i}| - \frac{\Delta\mathrm{x}}{2}}{\sigma_\mathrm{j}\sqrt{2}}\right) - \frac{\mathrm{c_j}}{2}\mathrm{erfc}\left(\frac{|\mu_\mathrm{j} - \mu_\mathrm{i}| + \frac{\Delta\mathrm{x}}{2}}{\sigma_\mathrm{j}\sqrt{2}}\right), & j \neq i \end{cases} \tag{4.36}$$

As μ approaches zero the Gaussian distribution of equation 4.34 begins to spill over into negative values, which in some cases may be unphysical. For instance, the Gaussian assumption leads to negative photons. We can chose to ignore this area or make the distribution more Poisson like by bouncing the Gaussian back at $\mu = 0$.

The formula for accounting for the area of the reflected Gaussian is described in 4.37. Ultimately this assumption has little impact on the S1 and S2 analysis because the threshold cut off well before the zero interface is reached, but it does make the distributions more Poisson like near the zeroth bins. Equation 4.37 is the same as 4.36 with the bin center μ_i mapped to $-\mu_i$.

$$\mathrm{B_{i,j}} = \frac{\mathrm{c_j}}{2}\mathrm{erfc}\left(\frac{|\mu_j + \mu_i| - \frac{\Delta x}{2}}{\sigma_j\sqrt{2}}\right) - \frac{\mathrm{c_j}}{2}\mathrm{erfc}\left(\frac{|\mu_j + \mu_i| + \frac{\Delta x}{2}}{\sigma_j\sqrt{2}}\right) \tag{4.37}$$

The error function and complementary error function are defined in equation 4.38 and the coefficient c_i is defined in equation 4.34.

$$\begin{aligned} \mathrm{erf(x)} &= \frac{2}{\sqrt{\pi}} \times \int_0^x \exp(-t^2) \\ \mathrm{erfc(x)} &= \frac{2}{\sqrt{\pi}} \times \int_x^\infty \exp(-t^2) = 1 - \mathrm{erf(x)} \end{aligned} \tag{4.38}$$

Finally, we solve for the observed mean in the i^{th} bin by summing all the Gaussian overlaps $A_{i,j} + B_{i,j}$ (equations 4.36,4.37), weighting the overlapping area from each bin by the corresponding bin center μ_j. The result is shown in equation 4.39 and is equivalent to equation 4.35 when the area from the reflected Gaussian is not considered, $B_{i,j}$=0.

$$\nu_i = \frac{\sum_{j=1}^{n} \mu_j \cdot (A_{i,j} + B_{i,j})}{\sum_{j=1}^{n} (A_{i,j} + B_{i,j})} \tag{4.39}$$

4.4.2 Smearing a Toy Spectrum

To demonstrate the application of equation 4.39 we use it to smear a toy linearly decaying spectrum. By modifying the dependence of σ_i on μ_i we can better understand the effects of the spectral shape and the functional for of the resolution.

Figure 4.17 shows the effect of the finite resolution on a linearly decaying spectral shape. Using a constant resolution σ the observed mean, when accounting for finite resolution, shifts down due to the spectral shape. In the case with $\sigma_i \sim \sqrt{\mu_i}$ the observed mean at first shifts higher as the increasing width at higher value bin centers, even with lower counts, out weighs the lower bin centers with higher counts and narrower widths. In both cases as the bin centers approach zero the observed mean shifts higher due to an imposed threshold at zero, here Poisson statistics take over and the Gaussian characterization leads to a loss of events below zero. Thus, for the sake of the toy model in figure 4.17 we only characterize the relation between the real mean and the observed mean from the second bin center. It is also worth mentioning that for the case of having a varying resolution in figure 4.17 the shift in spectral shape seems minor, yet there is a a significant 20% deviation in the observed mean of the last bin.

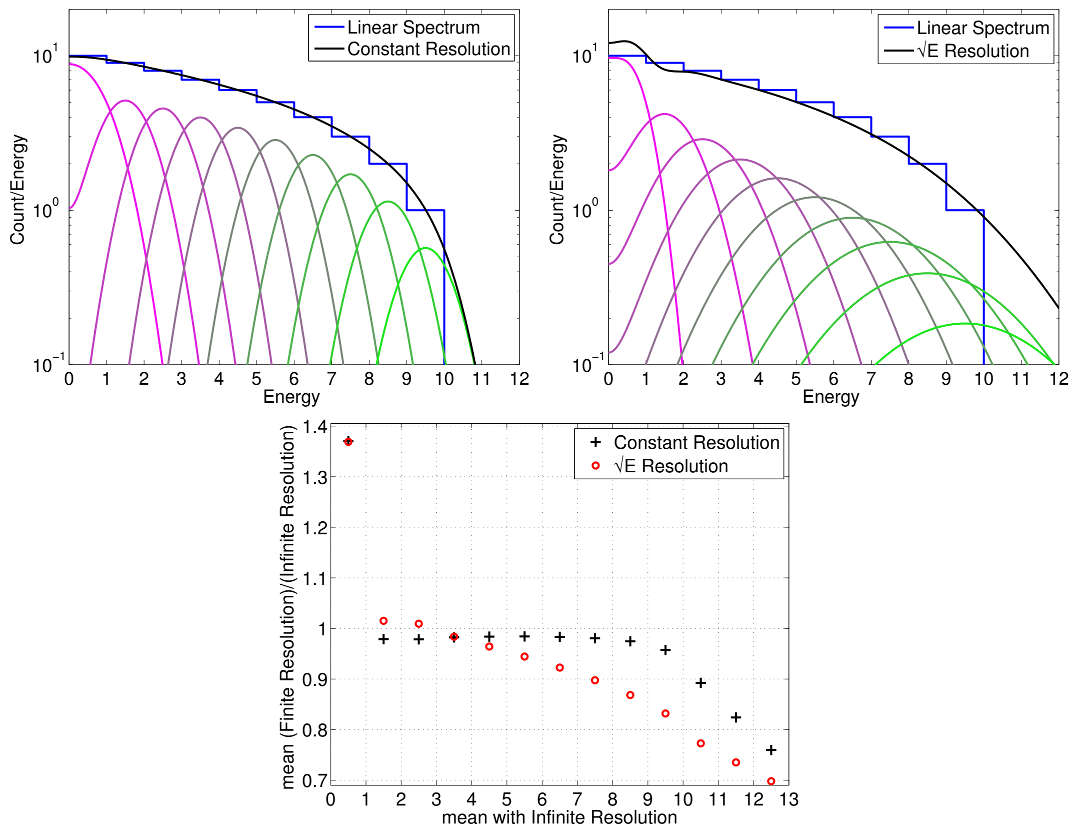

Figure 4.17: Top Left: A linearly decaying spectrum, in blue. The black curve represents the sum of the Gaussians assuming a constant resolution. Top Right: A linearly decaying spectrum, in blue. The black curve represents the sum of the Gaussians with a $\sqrt{\mathrm{E}}$ dependent resolution. Bottom: The observed mean, with finite resolution, compared to the real mean with infinite resolution. The black points are for the case with linear resolution and the red points represent the case with $\sqrt{\mathrm{E}}$ dependent resolution.

4.5 Measuring LY, QY and Recombination, Uncorrected for Spectral shape

4.5.1 Tritium S1 Mean and NEST

The correction for the mean of the measured light yield, S1 [Phe], for tritium beta decay can be solved for using equation 4.39. Starting with a simulated S1 tritium spectrum with infinite resolution and applying equations 4.34-4.39 one can attain the mapping of measured mean to true mean. The resolution of S1 was determined from statistical and instrumental fluctuations and is given in equation 4.12 and 4.13. The use of Gaussian error down to low S1 is an acceptable approximation since underlying distribution actually consists of the number of photons, $\mathrm{n}_\gamma = \frac{\mathrm{S1}}{\mathrm{g1}}$. With g1=0.097 there are still 20 photons near the S1 threshold of 2 [Phe], thus the Gaussian model is still a close approximation of the underlying Poisson distribution. We will use the Gaussian approximation as it makes the application of equations 4.34-4.39 much simpler. The variance in S1 is the result of recombination fluctuations, statistical fluctuations and instrumental fluctuations at a given energy. The functional form of all three have been previously measured and can be extrapolated for use with the tritium spectrum. The first step is to use the expected light yields from NEST along with the measured smearing from recombination and detector resolution to extract a correction factor for the observed S1 signal. Having a priori knowledge of light yields will allow for the spectral shape to be corrected or can at least be used to approximate an error when we go to extract the light yield and recombination fluctuations from the tritium beta spectrum.

$$\sigma_{\mathrm{S1}}^{2} = \mathrm{g}_{1}^{2}(\sigma_{\mathrm{n}_{\gamma_{\mathrm{stat}}}}^{2} + \sigma_{\mathrm{n}_{\gamma_{\mathrm{inst}}}}^{2} + \sigma_{\mathrm{R}}^{2}) \tag{4.40}$$

Figure 4.18 shows the application of smearing from equation 4.40 applied to the expected S1 tritium spectrum from NEST overlaid with the data. The mapping for converting the observed S1 to the real S1 is shown in figure 4.18. To calculate the correction we start with the NEST light yield, apply the measured g1, convolve it with a tritium beta spectrum and add in our first approximation of recombination fluctuations measured in equation 4.23, given infinite detector resolution this is the spectrum the LUX detector would observe in S1 space. Knowing the dependance of detector resolution vs. the number of photons of a given event (equation 4.14) we can apply the model as outlined in 4.4 and calculate the shift from observed mean photons to real mean photons.

4.5.2 Tritium S2 Mean and NEST

The correction for the mean of the measured charge yield, S2 [Phe], for tritium beta decay can be solved for using equation 4.39. Starting with a simulated S2 tritium spectrum with infinite resolution and applying equations 4.34-4.39 one can attain the mapping of measured mean to true mean. The resolution of S2 was determined from statistical and instrumental fluctuations and is given in equation 4.12 and 4.13. The use of Gaussian error down to low S2 is an acceptable approximation since the S2 spectrum ends at 300 [Phe], $\mathrm{n_e} = \frac{\mathrm{S2}}{\mathrm{g2}}$. With g2=5.75 there are still 50 electrons near

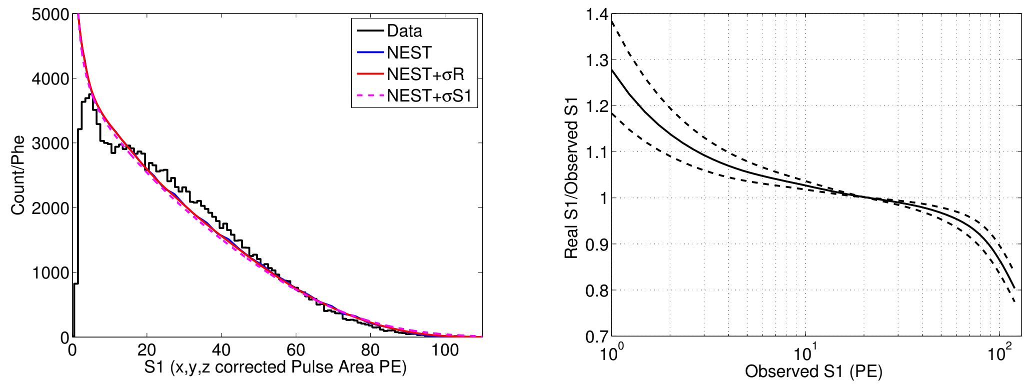

Figure 4.18: Left: In Black S1 tritium spectrum extracted from the data. In blue, The NEST light yield curve. In red, the NEST light yield curve with recombination fluctuations. Dashed magenta is NEST light yield with smearing from equations 4.40. Right: The ratio of the real mean to the observed mean vs. the observed mean for a tritium photon spectrum. Note the S1 threshold at about 3 Phe in S1.

end of the tritium spectrum, thus the Gaussian model is still a close approximation of the underlying Poisson distribution. We will use the Gaussian approximation as it makes the application of equations 4.34-4.39 much simpler. As in the case of the light yield, the variance in S2 is the result of recombination fluctuations, statistical fluctuations and instrumental fluctuations at a given energy. The functional form of all three have been previously measured and can be extrapolated for use with the tritium spectrum. We first use the expected charge yields from NEST along with the measured smearing from recombination and detector resolution to extract a correction factor for the observed S2 signal. Having a priori knowledge of light yields will allow for the spectral shape to be corrected or can at least be used to approximate an error when we go to extract the charge yield and recombination fluctuations from the tritium beta spectrum.

$$\sigma_{\mathrm{S2}}^2 = \mathrm{g}_2^2(\sigma_{\mathrm{n_{e_{stat}}}}^2 + \sigma_{\mathrm{n_{e_{inst}}}}^2 + \sigma_{\mathrm{R}}^2) \tag{4.41}$$

Figure 4.19 shows the application of smearing from equation 4.41 applied to the S2 tritium spectrum expected from NEST overlaid with the data. As with the S1 spectrum the correction is calculated using NEST for charge yield with the measured g2 applied, convolve it with a tritium beta spectrum and using our first approximation of recombination fluctuations measured in equation 4.23, given infinite detector resolution this is the spectrum the LUX detector would observe in S2 space. Having calculated the dependance of detector resolution vs. the number of photons of a given event (equation 4.14) we can apply the smearing as outlined in 4.4 and calculate the shift from observed mean photons to real mean photons. From the S2 spectrum, which is more peaked than the S1, we see the 20% discrepancy with the NEST charge yield model but it may also be an indication of the error in g1 and g2.

4.5.3 Tritium Energy Spectrum

The mapping of the observed energy to real energy was determined using a full simulation of tritium beta decay. The accuracy of the smearing model described in equations 4.34-4.39 can be tested by comparing it against the energy observed after a full NEST simulation. The energy depends on both S1 and S2 thus, mapping observed energy to true energy my be non trivial. Again, we start with a sim-

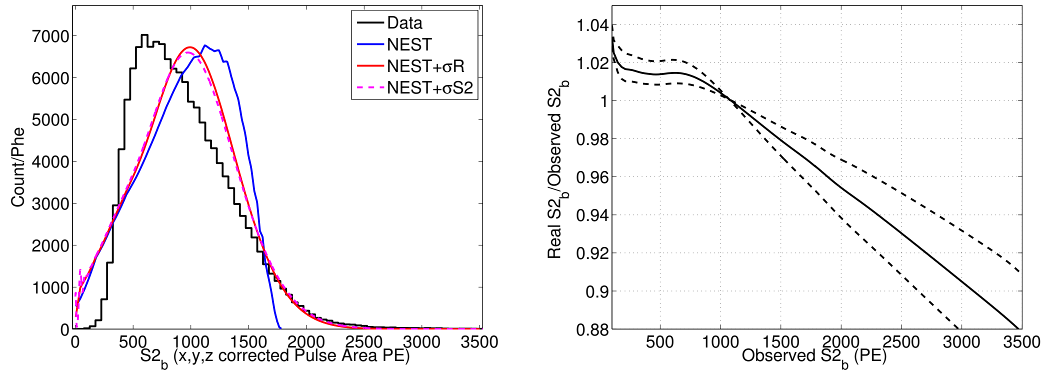

Figure 4.19: Left: In Black S2 tritium spectrum extracted from the data. In blue, The NEST light yield curve. In red, the NEST light yield curve with recombination fluctuations. Dashed magenta is NEST light yield with smearing from equations 4.41. Right: The ratio of the real mean to the observed mean vs. the observed mean for a tritium photon spectrum. Note the S2 threshold at about 400 Phe in S2.

ulated tritium energy spectrum with infinite resolution and apply the empirically determined resolution in equation 4.47, measured with ^{127}Xe X-rays and ^{83m}Kr calibrations. Figure 4.20 shows the comparison of smearing model vs true energy along with the smearing after running full photon and electron propagation in LUXSIM vs the true energy. The smearing form the model described in equations 4.34-4.39 is almost identical to the output of LUXSIM. The energy spectrum flares out at low energy, is pulled in from 5-10 [keV] and again flares out slightly above 15 [keV]. It is important to note that the change in the spectral shape is hardly noticeable, as was the case with S1 and somewhat with S2. Figure 4.21 shows the results for mapping observed energy to real energy using both smearing methods. The two methods show good agreement down to the threshold of 1.5 [keV], the agreement with simulation is always within 1%. Below 2 [keV] the model predicts the ratio of true energy to observed energy to rise as there are greater number of events at higher energy spilling over to lower energy, the simulation however does not show this behavior leading to a 5% discrepancy in the 1 [keV] bin. We take the difference between the smearing model and LUXSIM as a systematic uncertainty.

Using equation 4.30, 4.6 and 4.42 we solve for the the spread in E as a function energy 4.47. a_γ and a_e are the coefficients in front of the root n term on the n_γ and n_e statistical variance . W=73 $[\frac{\mathrm{N_{quanta}}}{\mathrm{keV}}]$.

$$\mathrm{E} = \frac{1}{\mathrm{W}}(\mathrm{n}_\gamma + \mathrm{n}_{\mathrm{e}^-}) \tag{4.42}$$

$$\sigma \mathrm{E}^2 = \frac{1}{\mathrm{W}^2}(\sigma \mathrm{n}_\gamma^2 + \sigma \mathrm{n}_{\mathrm{e}^-}^2) \tag{4.43}$$

$$\sigma \mathrm{E}^2 = \frac{1}{\mathrm{W}^2}(\mathrm{a}_\gamma^2 \mathrm{n}_\gamma + \mathrm{a}_\mathrm{e}^2 \mathrm{n}_{\mathrm{e}^-}) \tag{4.44}$$

$$\sigma \mathrm{E}^2 = \frac{(\mathrm{a}_\gamma + \mathrm{a}_\mathrm{e})^2}{\mathrm{W}} \frac{(\mathrm{n}_\gamma + \mathrm{n}_{\mathrm{e}^-})}{\mathrm{W}} \tag{4.45}$$

$$\sigma \mathrm{E}^2 = \frac{(\mathrm{a}_\gamma + \mathrm{a}_\mathrm{e})^2}{\mathrm{W}} \mathrm{E} \tag{4.46}$$

$$\sigma \mathrm{E} = \frac{(\mathrm{a}_\gamma + \mathrm{a}_\mathrm{e})}{\sqrt{\mathrm{W}}} \sqrt{\mathrm{E}} \tag{4.47}$$

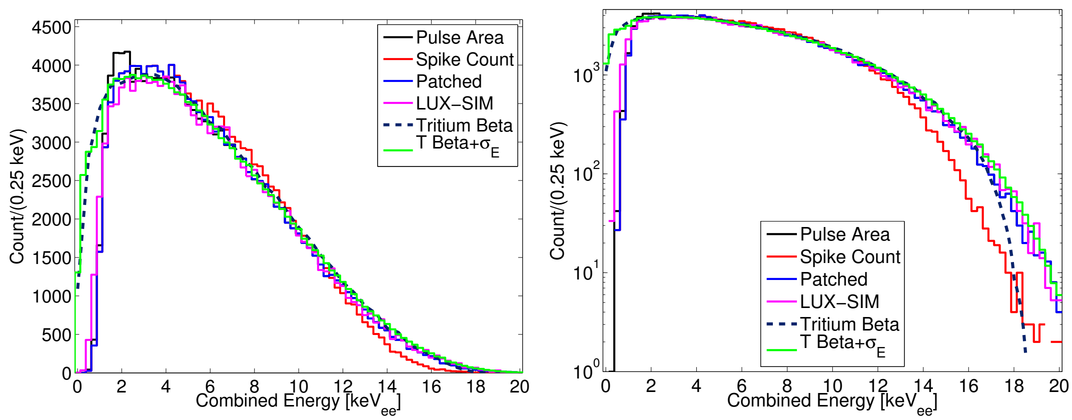

Figure 4.20: The tritium energy spectrum reconstructed from the data using both Pulse Area and Spike count for S1. Along with LUX SIM, the true tritium beta spectrum and a tritium spectrum smeared with detector resolution.

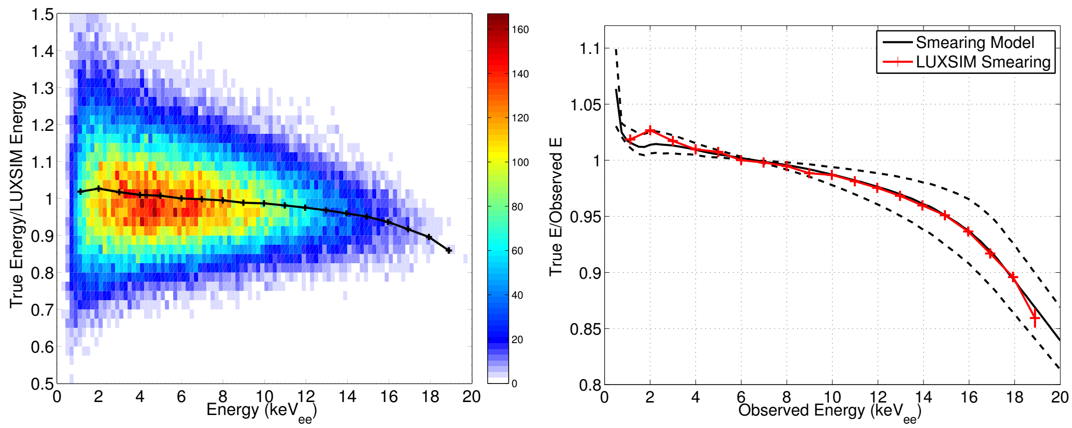

Figure 4.21: Left, mapping from real Monte Carlo energy to observed energy after applying a finite resolution using LUXSIM. Right, comparing the correction determined from the Monte Carlo (Red) to the detector smearing model (black) given in equation 4.47. The dashed lines represent the uncertainty in the measured value of F(E). The agreement is within errors from 1 to 18 keVee. The Energy threshold is near 1.0 keV$_{ee}$.

4.5.4 LY, QY, σR Result

The S1 and S2 spectral shape is not a good match with the light yield model from NEST, thus applying a correction to the observed means using NEST is not prudent. Fortunately, we see that both in the S1 and S2 region of interest were the majority of the tritium events occur the spectral shape correction is less than 10%. Further, the reconstructed energy, uncorrected for spectral shape, is go to within 10% as well. Knowing this we can move forward with extracting a more accurate light yield and recombination fluctuation accepting the small error in order to create a more accurate model than NEST to which then we can apply the spectral shape correction.

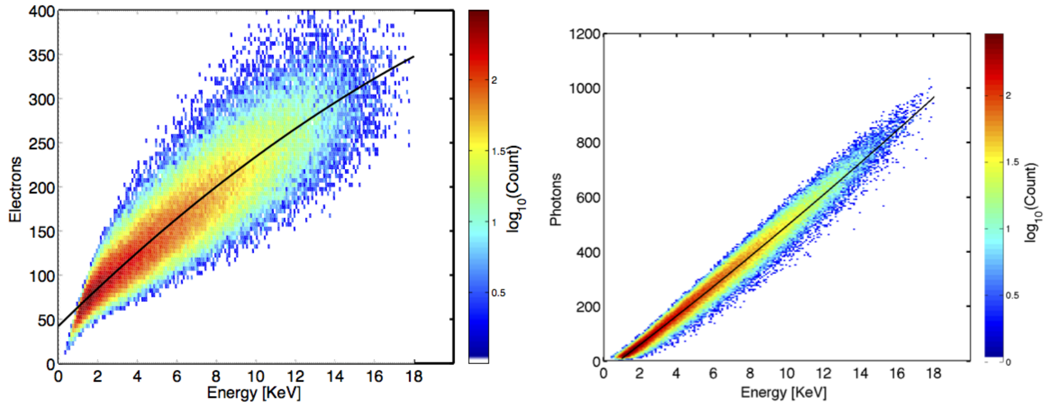

Figure 4.22: Number of photons (left) and electrons (right) vs. energy from tritium data without spectral shape correction. The spread in quanta per energy bin is used to measure recombination fluctuations.

Having extracted light yield (Photons/keV] and charge yield (electrons/keV) we compare the initial result from the tritium data to NEST, and is shown in figure 4.24. The disagreement between the data and the NEST yields was expected since previously the S1 and S2 tritium spectrum did not line up, in the previous section. Though the means do not match the measured light yield is within 1 sigma considering the large error in gains g1 and g2.

4.6 Measuring LY, QY, Recombination, Corrected for Spectral shape

In the previous section we determined that the NEST model was not sufficient to produce a spectral shape correction for the tritium data. However, it was shown that and spectral shape correction is sufficiently small (less than 10%) to extract light yield, charge yield and recombination from the tritium spectrum, using this information the model was improved and new simulations were produced. In this section we will take the information gathered in the previous section and apply the known detector resolution in order to create a spectral shape correction for the tritium S1 and S2. Having an improved model for NEST we can even determine the efficiency for detecting tritium S1, S2 and the energy threshold, since the tritium spectrum still provides events well below the expected energy threshold of around 1.5 keV_{ee}.

4.6.1 Tritium S1 Correction

Figure 4.25 shows the application of smearing from equation 4.40 applied to the light yield extracted from the uncorrected tritium data with the data. The mapping for converting the observed S1 to the real S1 is shown in the figure. To calculate the correction we start with the extracted light yield, apply the measured g1, convolve it with a tritium beta spectrum and add in our first approximation of recombination fluctuations measured in equation 4.23, given infinite detector resolution this is the spectrum the LUX detector would observe in S1 space. Knowing the dependance of detector resolution vs. the number of photons of a given event (equation 4.14) we can apply the model as outlined in 4.4 and calculate the shift from observed mean photons to real mean photons.

4.6.2 Tritium S2 Correction

Figure 4.25 shows the application of smearing from equation 4.41 applied to the charge yield extracted from the uncorrected tritium data with the data. The mapping for converting the observed S2 to the real S2 is shown in the figure. To calculate the correction we start with the extracted light yield, apply the measured g2, convolve it with a tritium beta spectrum and add in our first approximation of recombination fluctuations measured in equation 4.23, given infinite detector resolution this is the spectrum the LUX detector would observe in S1 space. Knowing the dependance of detector resolution vs. the number of electrons of a given event (equation 4.14) we can apply the model as outlined in 4.4 and calculate the shift from observed mean photons to real mean photons.

4.7 Thresholds

4.8 Ionization and Scintillation Yield and Recombination After Correction

4.9 The Standard Candle. Light Yield from ^{83m}Kr

Quenching of scintillation yield vs. field has been typically defined relative to 32.1 keV decay of ^{83m}Kr at zero field [?],[?]. ^{83m}Kr first emits a 32.1 [keV] gamma followed by a 9.4 [keV] with a half life of 154 [ns] between the two (refs). The combined signal (41.6 [keV]) is found by the pulse finder in the majority of cases, using the standard WIMP search pulse gap setting of 500 ns. However, the combined signal is not useful as a standard calibration since the light yield from the second 9.4 keV decay depends strongly on decay time separation. The second 9.4 keV decay is effected by the presence of exitons from the initial 32.1 [keV] decay. See figure [show LUX result]

Fortunately, the first 32.1 keV appears to have no time dependance as it decays in 'relaxed' xenon without the presence of additional exitons [?]. For purposes of light yield normalization at zero field the 32.1 keV gamma serves as a good low energy standard candle for xenon detectors.

There were two data sets in late 2013 that contain ^{83m}Kr decays at zero field. Since the S2 (charge) signal is unavailable the top-bottom asymmetry, $\frac{top-bottom}{top+bottom}$, is used to define the Z coordinate for position dependent corrections. The XY correction is subdominant to the Z dependent correction for light yield. Figure [] shows the linear mapping from top-bottom asymmetry to detector depth (Z). With the Z correction applied the average pulse area (Phe) normalized to the detector center (241.6 mm below the gate grid) is found to be 267.4 $\pm^{\text{stat}}$ 1.5 $\pm^{\text{sys}}$ 5. See Figure 4.31.

4.9.1 Field dependence of light yield from the 32.1 keV gamma of ^{83m}Kr

Charge separation increases with drift field leading to less recombination for light production, causing scintillation yield to be quenched. See table 4.5 for a list of the measured scintillation of the 32.1 keV gamma from ^{83m}Kr, also includes the NEST predictions.

Field [V/cm]	S1[Phe]	Photons[n_γ]	Yield [n_γ/keV]	NEST [n_γ/keV]
0	267.4 ± 6.5	1980 ± 40.7	61.7 ± 1.27	64.2 ± 2.6
51	246.7 ± 1.2	1827.4 ± 8.9	56.9 ± 0.28	60.8 ± 2.5
105	233.6 ± 1.4	1730.4 ± 10.4	53.9 ± 0.32	58.3 ± 2.3
182	212.3 ± 1.3	1572.6 ± 9.6	49.0 ±0.30	54.9 ± 2.1

Table 4.5: Field dependance of the light yield form the 32.1 keV decay of ^{83m}Kr. The fields are calculated using a two dimensional model and not accounting potential charge accumulation on inner teflon panels.

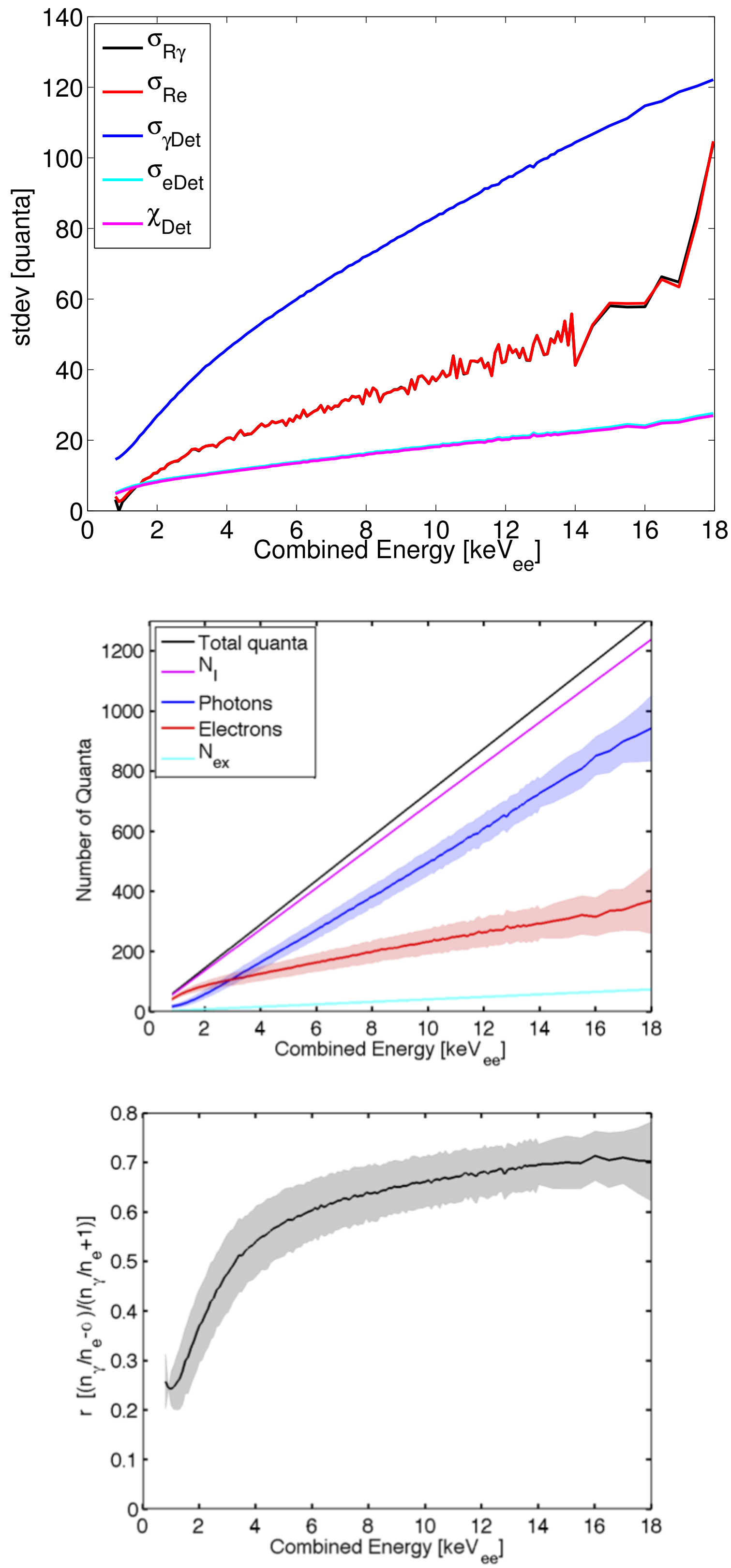

Figure 4.23: Top: Extracted recombination fluctuation from the tritium data from fluctuations in photons and electrons (Black and Red receptively). Bottom right: mean number of quanta in photons, electrons, ions, exitons vs. energy [keV] for

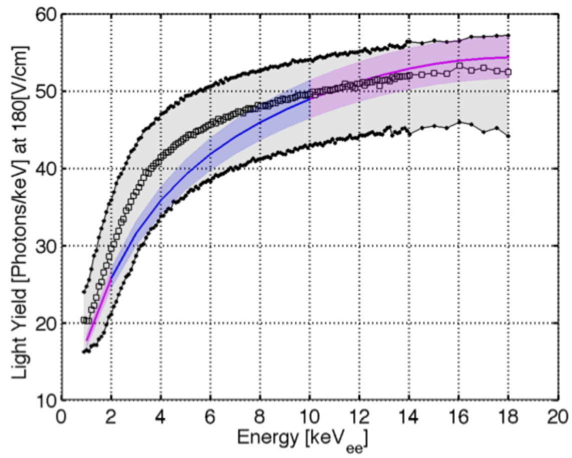

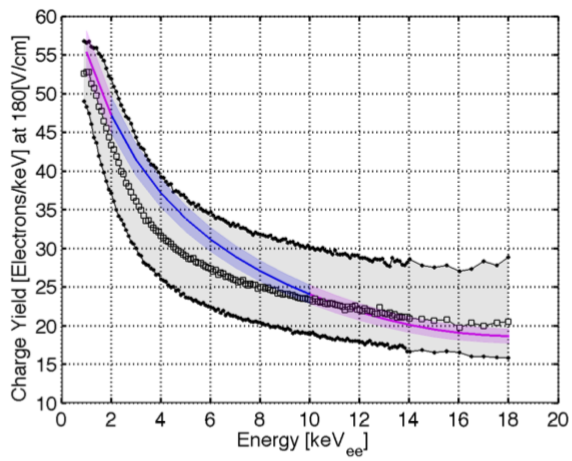

Figure 4.24: Light yield and charge yield from tritium data without spectral shape correction at 180 [V/cm] in black, the shaded region represents the one sigma uncertainty on g1 and g2. The NEST yield prediction and it's corresponding 1 sigma is shaded in blue. NEST interpolation in show in magenta to energies where the model is not vetted.

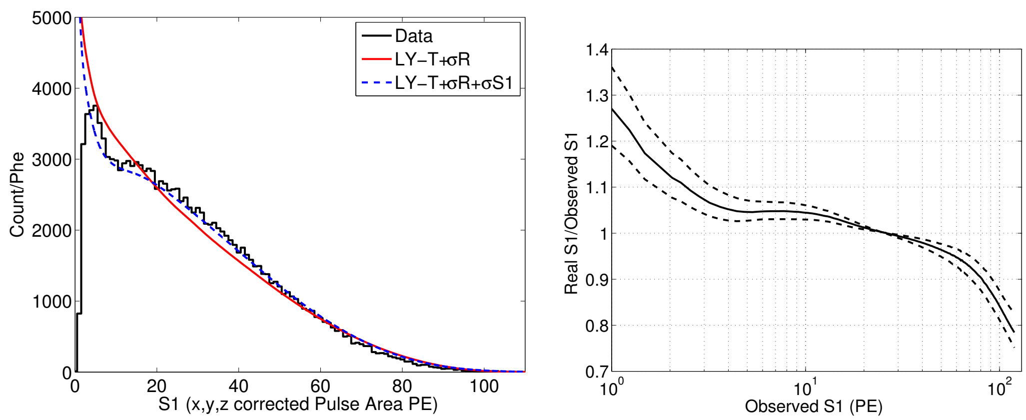

Figure 4.25: Left: In Black, tritium data. In red, the spectrum after applying measured recombination fluctuations. In dashed blue is after applying recombination and finite detector resolution of equation. Left: Mapping of the observed mean, with finite resolution, to the mean with infinite resolution for a tritium photon spectrum. Bottom Right: The ratio of the real mean to the observed mean vs. the observed mean for a tritium photon spectrum. Note the S1 threshold at about 3 Phe in S1.

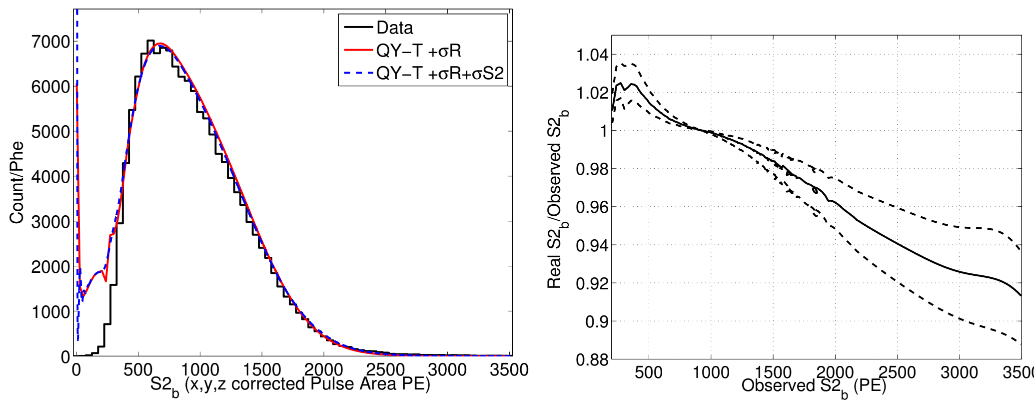

Figure 4.26: Left: In Black, tritium data. In red, the spectrum after applying measured recombination fluctuations. In dashed blue is after applying recombination and finite detector resolution of equation. Left: Mapping of the observed mean, with finite resolution, to the mean with infinite resolution for a tritium photon spectrum. Bottom Right: The ratio of the real mean to the observed mean vs. the observed mean for a tritium photon spectrum. Note the S2 threshold at about 400 Phe.

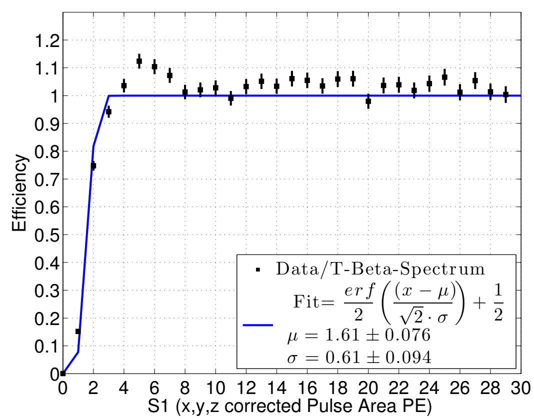

(a) S1

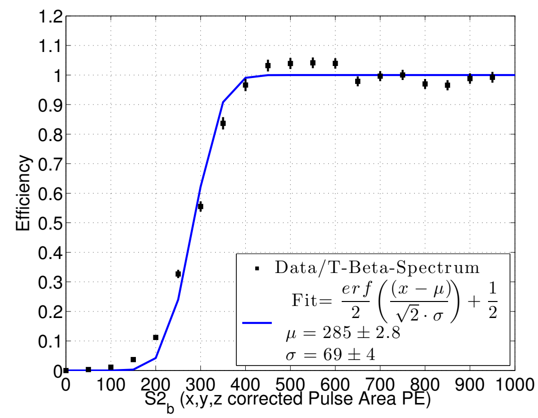

(b) $S2_b$ (golden)

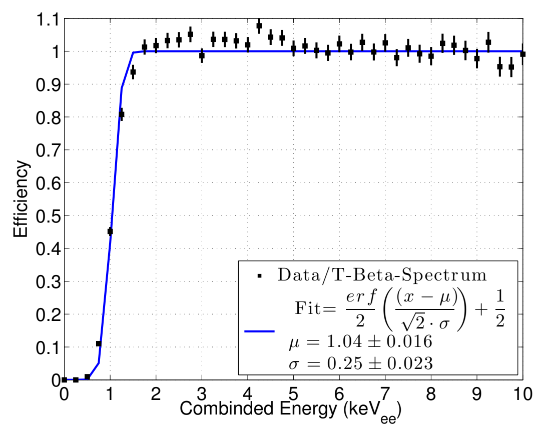

(c) Combined Energy

Figure 4.27: Threshold calculated from difference of simulated Tritium S1, S2 and energy spectra. a) S1 b) $S2_b$, c) E .

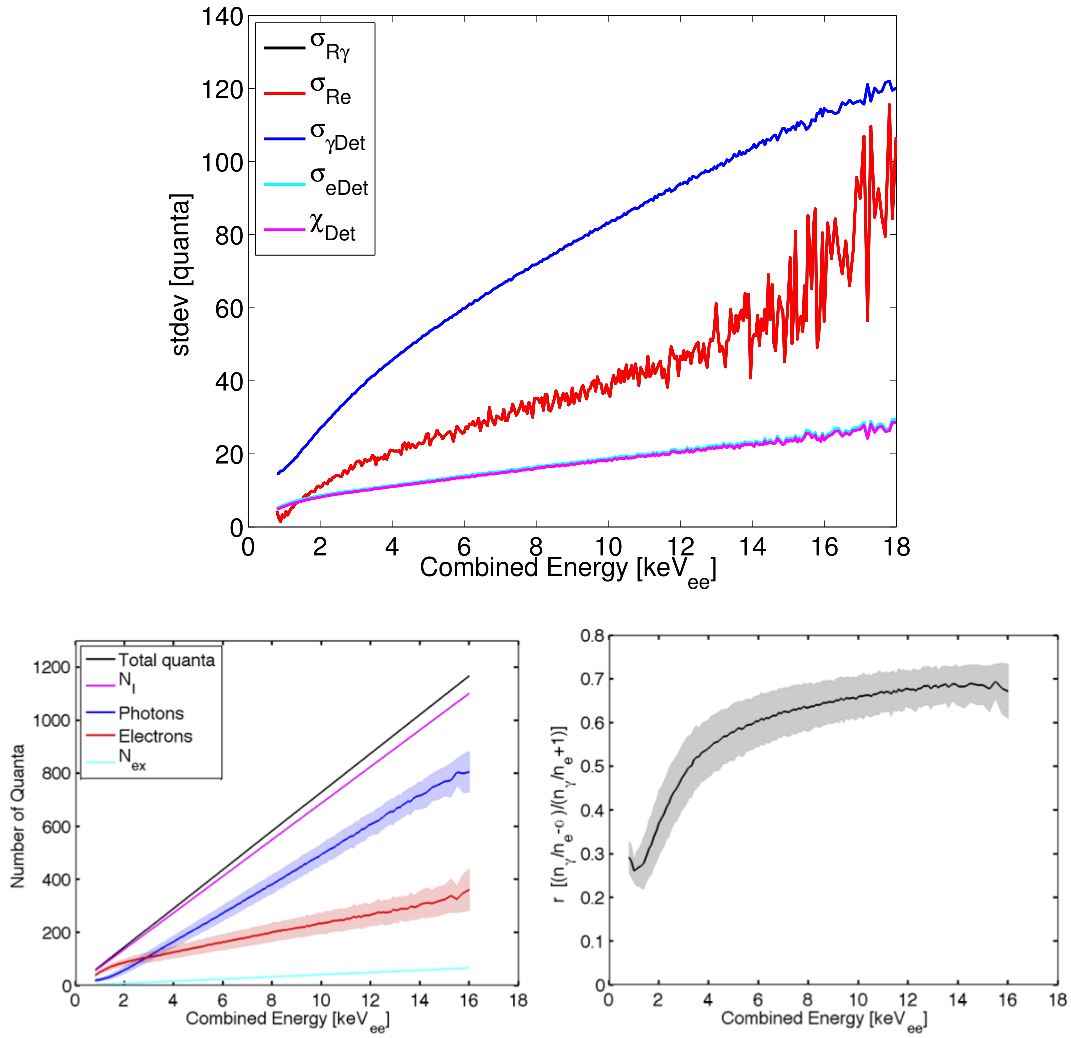

Figure 4.28: After spectral shape correction. Top: Extracted recombination fluctuation from the tritium data from fluctuations in photons and electrons (Black and Red receptively). Bottom right: mean number of quanta in photons, electrons, ions, exitons vs. energy [keV] for the tritium calibrations. Bottom left: Recombination fraction and the one sigma (shaded) vs. energy [keV].

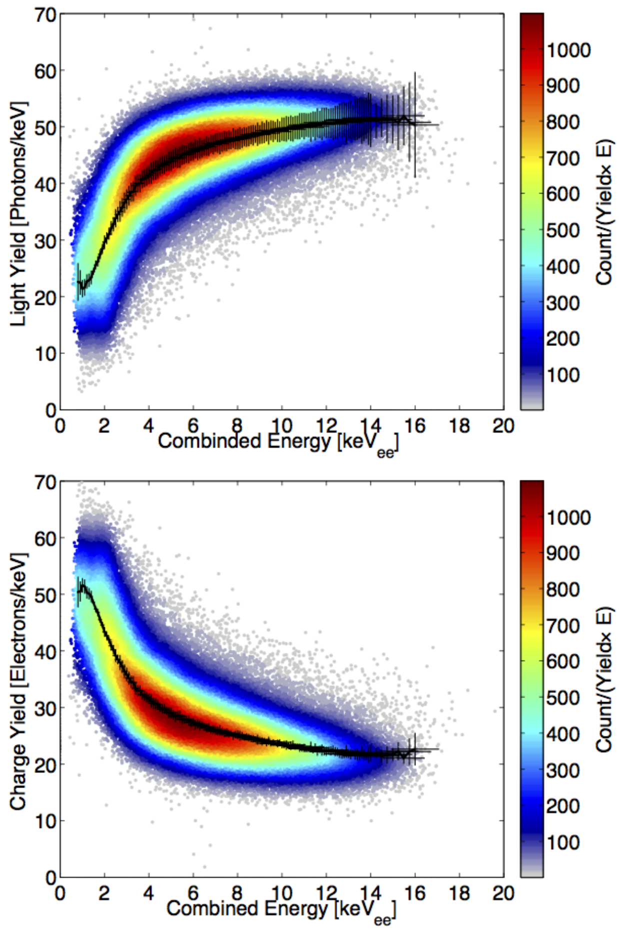

Figure 4.29: Extracting LY and QY from data corrected for spectral shape.

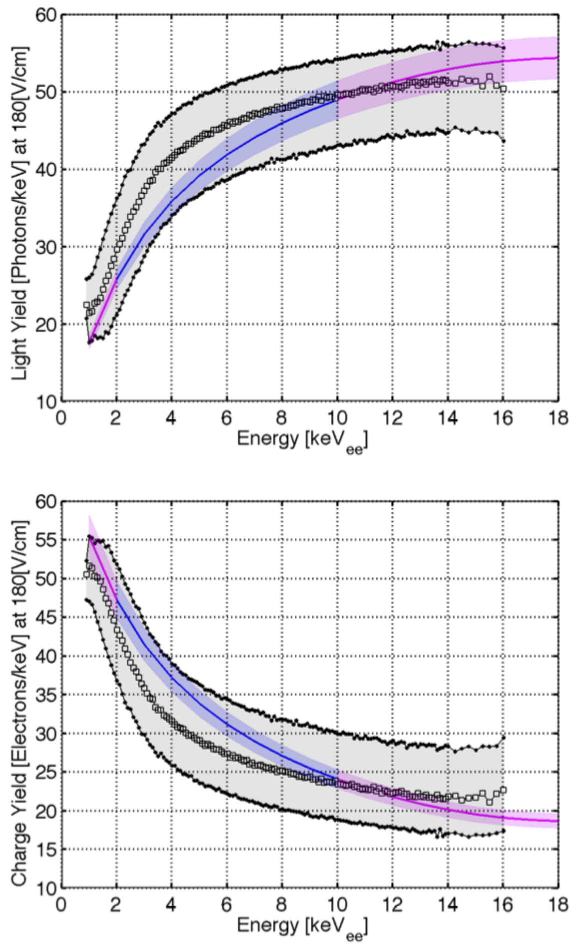

Figure 4.30: LY and QY from tritium data corrected for spectral shape along with the 1 sigma band of g1/g2. The blue and magenta curve are NEST extrapolation and interpolation, respectively.

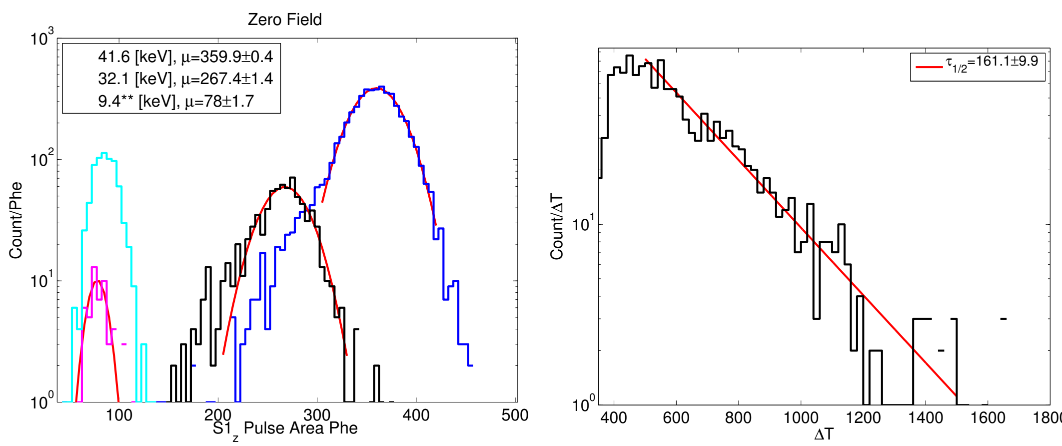

Figure 4.31: Left: ^{83m}Kr peaks at zero field. ** The 9.4 keV peak is fit only for events with a decay time separation greater than 1000 [ns]. Right: shows the timing separation between the 32.1 and 9.4 [keV] decays plotted above.